MASTER IN PHYSICS

Under Fire : Simulating the impact of radiation summarization

PERROT, Alexandre

Award date:
2023

Awarding institution:
University of Namur

ADINETA VAGA UNDER FIRE: SIMULATING THE IMPACT OF RADIATION

by

Perrot Alexandre

A Master's Thesis

Submitted to the Department of Physics

Namur University

In Partial Fulfillment of the Requirements

For a Master's Degree

June 2023

Acknowledgements

I am grateful to Boris Hespeels for recognizing the value in my thesis results and took the initiative to contact a journal for potential publication. I am particularly grateful for Boris Hespeels's skill in identifying aspects of the research and result in which I was the most uncomfortable discussing or addressing. His ability to bring these sensitive subjects combined with his expertise helped improve my communication skills and made me think critically on the research results. I would also like to express my gratitude for the open-door policy Boris Hespeels maintained in his laboratory. The trust he placed in me by providing access whenever needed allowed me the freedom and flexibility to work at my convenience.

I would like to express my gratitude towards my thesis promoter, Anne-Catherine Heuskin, for her guidance and support throughout the completion of my master's thesis. Her expertise and feedback greatly contributed to the refinement of my master’s thesis. I am grateful for Anne-Catherine Heuskin's calm and understanding approach regarding deadlines and time management. Her support and flexibility created an environment where I could focus on my research without undue stress.

To Manon, thank you for being an immutable source of support and encouragement during the highs and lows the academic endeavor. The precious moments we shared together on weekends served as a replenishing source of energy. Furthermore, I am grateful for your loving complaints during weekdays when I inadvertently neglect to communicate. Without your insistence on nurturing our relationship, I might have ended isolating myself and dedicating all my time to work. I sincerely hope that you will never stop to sulk for that in the future.

To my family, for your encouragement and support. Your unwavering belief in my abilities, even when I embark on unconventional or audacious endeavors. Their confidence in me has served as a much-needed counterbalance to my own occasional self-doubt.

Introduction

The bdelloid rotifers are unique microscopic animals found worldwide, characterized by their apparent absence of males (Maynard Smith 1986; Judson et Normark 1996; Segers 2007). They have a remarkable ability to survive desiccation and exhibit resistance to various stresses (C. Ricci et al. 2005; Fischer et al. 2013; C. Ricci 2017; E. Gladyshev et Meselson 2008; Hespeels et al. 2023). Studies have shown that the rotifer bdelloid *Adineta vaga* can survive extreme radiation doses, which sparked interest in understanding their radiation resistance. Previous research demonstrated that desiccated bdelloid rotifers could withstand radiation doses exceeding 5000 Gray[1], while mammalian cells typically succumb to doses ranging from 2 to 6 Gray (Hespeels et al. 2020). However, the mechanisms underlying their extraordinary radiation resistance remain unclear. It is hypothesized that the ability to repair massive DNA damage accumulated during desiccation contributes to their radiation resistance (E. A. Gladyshev et Arkhipova 2010; Hespeels et al. 2014).

In a study conducted by (Hespeels et al. 2020), the effects of 4 MeV protons, 0.5 GeV/nucleon ^{56}Fe, and X-rays on the survival and fertility of *A. Vaga* individuals were examined. The rotifers were exposed to doses ranging from a few hundred to thousands of Grays, and the outcomes were interpreted differently based on survival and fertility. While the individuals could survive even the most extreme doses, much lower levels of radiation were sufficient to sterilize them. Sterilization threshold for 50% of the population were observed at approximately 1,035 Gray for X-rays, 453 Gray for protons, and 461 Gray for Fe particles. As the exposure to radiation increases, a greater number of nuclei in individuals are damaged. Eventually, if all the nuclei are damaged, it leads to complete sterilization of the population. However, it is unclear if the thresholds for sterilization in relation to radiation exposure is associated with (1) a statistical absence of damage or (2) the quantity or complexity of the damage. To investigate this question, it is crucial to determine at which dose all nuclei are undoubtedly damaged. To explore the targeting and impact of radiation on bdelloid rotifers, this study employs the simulation tool TOPAS, based on Geant4. The objective is to identify the individuals and cells that are effectively targeted by radiation, thereby enhancing the interpretation of bdelloid radiation data, and ruling out the possibility of untargeted individuals or cell types in the dose range used. Furthermore, comparisons between low and high linear energy transfer (LET) radiations are conducted to gain further insights into the findings.

Adineta vaga's exceptional resistance to ionizing radiation positions it as an ideal model organism for investigating the effects of microgravity and ionizing radiation in space environments. The UNamur, ULB and the Belgian Nuclear Research Centre SCK CEN, in collaboration with funding from the European Space Agency (ESA) and the Belgian Federal Science Policy Office (BELSPO), carried out two space missions known as Rob-1 and Rob-2. These missions were part of the RISE project (Rotifer in space) and focused on studying the irradiation of rotifers aboard the International Space Station (ISS) (website: rotifer-in-space.com). Currently, there is a third mission called Rotifer-A in the development phase, which aims to investigate the irradiation of rotifers using a carrier module placed on an external facility of the station. This mission is part of a larger project that involves the construction of a

[1] Gray (or Gy) is a measure of the energy deposited by the radiation in a given mass.

custom exobiology facility named EXPO, inspired by the existing EXPOSE facility. The EXPOSE facility is situated on the exterior of the European Columbus model of the ISS and serves the primary purpose of exposing various biological samples to the extreme conditions encountered in space (Rabbow et al. 2015; 2017). One of the notable experiments conducted on the EXPOSE facility is Expose-R, where a total of 1220 samples ranging from unicellular organisms to mosquito larvae and seeds were exposed to space conditions for durations of up to 22 months (Rabbow et al. 2015). Following the design of the EXPOSE facility, biological samples will be placed in modular carriers, which will be then stacked within cavities and protected by magnesium fluoride or quartz windows. Density filters may also be employed to partially reduce the exposure of the samples to space conditions.

Studying space radiation is a complex undertaking due to the presence of diverse and dynamic radiation sources, which can be unpredictable. Additionally, it is challenging to experimentally determine the specific contribution of each radiation source to the total dose. While certain aspects of the space environment, such as the effects of vacuum, solar UV radiation, and temperature on bdelloids, can be studied on the ground using tools like the UNamur LARN research facility space vacuum simulator, there is currently a lack of available information regarding the effects of cosmic radiations on rotifers. As a result, the use of simulation tools becomes appropriate as they can replicate the mission's geometry and facilitate the examination of individual contributions from different sources.

This master thesis is divided in three sections. The first section provides a comprehensive theoretical overview of the subject, delving into the concepts of ionizing radiation, space environments, and the interactions of radiation in matter. This part also introduces the Geant4 simulation toolkit, which forms the basis for the Topas software utilized throughout this work.

The second section incorporates a scientific paper currently revised for publication in Hydrobiologia. It focuses on a study aimed at determining the radiation thresholds required for complete coverage of individuals or nuclei. The section provides detailed descriptions of the modeling and implementation of bdelloid rotifers and experimental setups in the Topas software. It also presents the radiation coverage achieved at the simulated radiation thresholds, along with an examination of the differences in coverage between radiation with different ionization densities. The section concludes with a discussion on potential future research directions and the biological implications of the obtained results.

The third section delves into the research conducted on the future Rotifer-A experiment, which aims to expose desiccated rotifers to space environments. It covers the utilization of Oltaris, an online tool for retrieving space environment data, and its implementation in Topas. Furthermore, the section explores the incorporation of complex geometries into Oltaris to extract additional valuable information using ray-tracing algorithms. The simulated radiation doses experienced by the space-exposed samples are also exposed. The section concludes with a thorough examination of the differentiation of various contributions and an in-depth discussion of their implications.

The thesis concludes with a forward-looking discussion, offering perspectives on potential future directions of this research.

Section 1: Physical concepts

In this first section, the concept of ionizing radiation and space radiation environments are discussed. Then, the various ionization processes and interactions that can occur in matter will be reviewed for all radiation types. The impact of radiation on living matter will be shortly discussed before reviewing how physics is handled in the Geant4 simulation toolkit.

Ionizing radiations and space environment

Ionization occurs when atoms become electrically charged, which can lead to the breakage of chemical bonds and ultimately cause damage to biological structures such as cells, organs, and organisms (Nikjoo, Uehara, et Emfietzoglou 2016; Leroy et Rancoita 2016). Radiation is the propagation of energy through space by particles or waves. Some radiation are ionizing, meaning that they can ionize matter by depositing high energy amounts. The amount of energy required to ionize matter depends on its nature and structure. The dose quantifies the amount of energy deposited in matter and is expressed in *Gray* or *Gy*. Mathematically, the dose is the ratio between the deposited energy (E in *Joule*) and the mass of the considered volume (m in *kg*): $Dose(Gy) = E/m$. Ionizing radiation can be electromagnetic or corpuscular. On one hand, electromagnetic radiation carries energy through electromagnetic waves made up of photons. The energy of these photons is related to the frequency of the electromagnetic field oscillation by the Planck-Einstein relation $E=hv$, where E is the energy measured in Joules, $h \approx 6.63 \times 10^{-34}\, J.s$ the Planck constant and v the frequency, in hertz. The electromagnetic spectrum on Fig.1 illustrates the frequencies and therefore energies of electromagnetic radiation. These frequencies are generally divided into non-ionizing and ionizing radiation based on a mean ionization threshold for living matter. Electromagnetic ionizing radiation are far ultraviolet (starting at $v \sim 10^{16}$ Hz), X-rays and gamma rays (γ) (Perez 2017).

On the other hand, corpuscular radiation transports energy with massive particles, such as electrons, protons, neutrons, or heavier ions. All corpuscular radiation can ionize if the particles have sufficient energy. Heavy ions can fragment and create secondary ionizing particles.

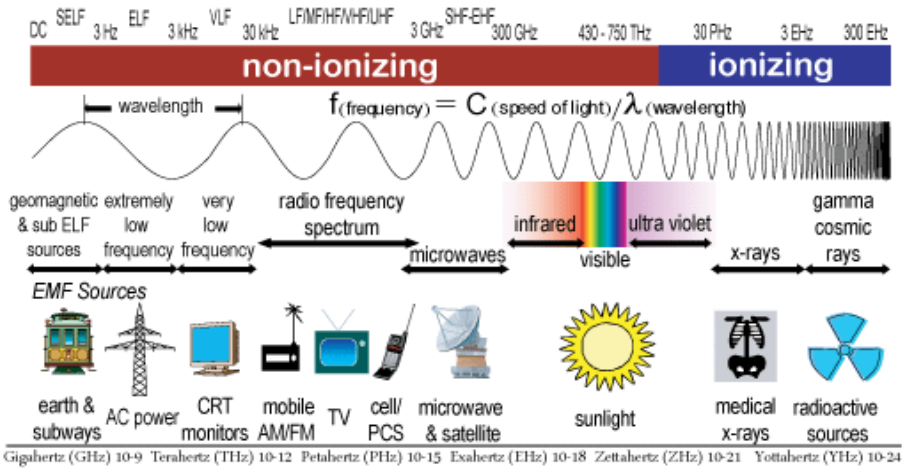

Fig. 1 Electromagnetic spectrum with non-ionizing and ionizing radiation separation. As the ionization threshold is dependent on the matter traversed, the demarcation between ionizing and non-ionizing is not absolute (Yong, Rahman, et Chew 2015).

Most ionizing radiation, electromagnetic and corpuscular, are produced during radioactive disintegration, while ionizing X-Rays are usually produced artificially, by firing electrons in a material, generally tungsten, copper, or molybdenum (Leroy et Rancoita 2016; Nikjoo, Uehara, et Emfietzoglou 2016; Penninckx 2023). The slowing of electrons in matter emits X Rays according to the bremsstrahlung phenomenon. The creation of ionizing radiation will be discussed in the context of space environment radiation.

The space environment beyond the Earth's atmosphere is abundant in ionizing radiation from various sources, which vary greatly in intensity. The energy spectrum of the massive radiation can range from 400 to 600 MeV per nucleon, while photon radiation covers the entirety of the electromagnetic spectrum, both ionizing and non-ionizing (Chancellor et al. 2021). The spatial radiation environment is typically divided into three categories: The Galactic Cosmic Rays or GCR, the sun (with solar winds and Solar Particle Events) and the particles trapped in the Earth's magnetic field (Chancellor et al. 2021).

The constant background of radiation outside the terrestrial atmosphere is referred to as GCR. These particles are fully ionized and are likely to originate from explosive events such as supernovae, primarily from within the Milky Way. They consist of a relatively constant proportion of 87% protons, 12% alpha particles, and ~1% heavy ions, traveling near the speed of light (Chancellor et al. 2021; O'Neill 2006). Additionally, GCR can produce a variety of secondary light particles such as neutrons, muons, pions or gammas when interacting with the ground or atmosphere of celestial bodies (Singleterry et al. 2010). The GCR flux varies inversely with the ~11-year solar cycle, with dose rates of 50 to 100 mGy/year at the maximum of solar activity and 150 to 300 mGy/year at the minimum of solar activity when measured at the altitude of the International Space Station (ISS) (Chancellor et al. 2021). The particles found in GCR are likely accelerated during supernovae explosions, during which the GCR particles are ionized and attain speeds comparable to that of light. There are other possible sources of GCR radiation, such as gamma-ray bursts or supermassive blackholes jets (Biermann et Sigl 2002; Schlickeiser 2010).

The Sun emits a wide range of frequencies, including visible light, infrared and ultraviolet radiation (« NASA - Space Radiation Analysis Group (SRAG) Web Site » 2023). The sun's emission is comparable to that of a black body with a temperature of 5,800 K. The corona (i.e., the outermost layer of the sun's atmosphere, comprised of plasma) is a source of ionizing ultraviolet light and X-rays that make only a small portion of the solar spectrum. However, at times, massive explosions known as solar flares occur on its surface, resulting in the release of enormous amounts of energy into space in the form of X-rays, gamma rays, and streams of protons and electrons. These Solar Particle Events or SPE are associated with unpredictable magnetic instabilities (Jiggens et al. 2014) and vary in frequency with the solar activity 11 year cycle (see Fig. 2a). Inside the ISS, these protons can produce dose rates up to 1500 mGy/hour. The 1989 October SPE is the largest event which has been well recorded by various space-based sensors (Jiggens et al. 2014). The differential proton fluxes from October 1989, due to the SPE, is illustrated in Fig. 2b. The SPE occurred around the 20 October and lasted several days. Solar winds are the last component of sun radiation and are composed of low-energy

protons and electrons, alpha particles, and small amounts of heavier ions such as C, N, O, Ne, Mg, Si, S and Fe. Their intensity is related to the solar cycle, although they are less energetic than the GCR (« NASA - Space Radiation Analysis Group (SRAG) Web Site » 2023). They are produced in a constant stream by the sun but cannot easily penetrate the Earth's magnetic field. Some particles, mainly protons, become trapped in the Earth's magnetic field, in a region known as the Van Allen belt. In the low orbit where the ISS is situated, at around 400 km of altitude, the station periodically passes through this region.

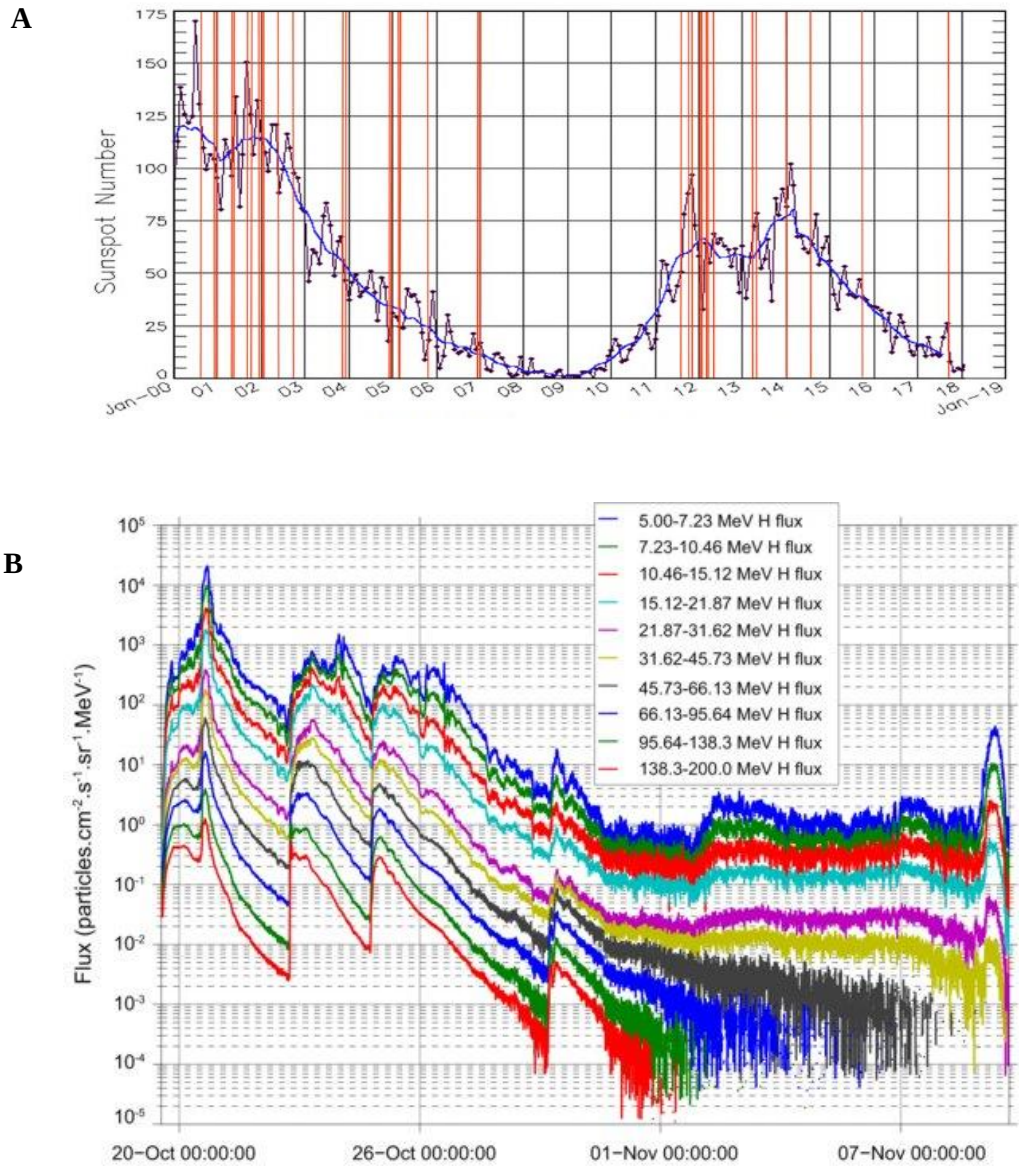

Fig. 2 Fig 2a is an illustration of the solar cycle. Year in abscissa and Sunspot (way of quantifying solar activity) in ordinate. The blue line is the smoothed average of sunspots, vertical lines are each time the SRAG (Space Radiation Analysis Group) was called into mission control due to an SPE event (« NASA - Space Radiation Analysis Group (SRAG) Web Site » 2023). From the cycle activity we can conclude that the years around 2025 will witness high solar activity. Fig 2b represents the proton flux during the solar particle event that occurred in October 1989. High, abnormal levels of highly energetic protons were recorded for several days, with a maximum around the 21st of October (Jiggens et al. 2014).

Ionization and radiation attenuation in matter

Understanding how ionizing radiation sources in space interact with matter is crucial. The nature of the particle, whether it's a photon, neutron, proton, or heavy ion, determines how these radiations interact and ionize matter. Charged particles can directly ionize atoms through Coulomb interaction, making them directly ionizing. On the other hand, neutral particles such as photons and neutrons can indirectly ionize atoms through non-Coulombian interactions, making them indirectly ionizing. Both types of ionizations can create secondary particles that can potentially play a significant role in the total irradiation output. The information presented here draws heavily from the works of Leroy et Rancoita 2016; Nikjoo, Uehara, et Emfietzoglou 2016; Penninckx 2023.

Photons are indirectly ionizing particles that can undergo five different interactions in matter, each with a specific probability of occurrence. In these interactions, most of the photon energy is transferred to an electron, causing it to oscillate or ionize it. Ionized electrons, with sufficient energy, can create additional ionizations. The five possible interactions for photons include the photoelectric effect, Compton scattering, pair production, Thomson-Rayleigh scattering, and photonuclear reactions, with the first four being drawn schematically in Fig. 3c. The photoelectric effect occurs when a photon is absorbed by an atom's electron, causing it to be ejected. The probability of this interaction, μ_{photo}, can be calculated using the following formula:

$$\mu_{photo} \propto \frac{Z^5}{(h\nu)^{\frac{7}{2}}}$$

With Z the atomic number of the traversed matter, $h \approx 6.63 \times 10^{-34}\ J.s$ the Planck constant and ν the photon frequency. The photoelectric effect is consequently more likely to occur for low energy photons in a heavy material.

Compton scattering is an elastic diffusion process in which an incoming photon collides with an electron. The electron is expulsed from the atom at an angle ϕ, and a photon of lower energy than the original is re-emitted at an angle θ (see Fig. 3c). The probability of Compton interaction $\mu_{Compton}$ is solely proportional to the inverse of the photon energy $h\nu$:

$$\mu_{Compton} \propto \frac{1}{h\nu}$$

When an incident photon has an energy greater than 1.022 MeV, twice the mass of an electron, it can produce an electron-positron pair. The positron will quickly annihilate upon encountering an electron, resulting in the production of two gamma rays. The probability of pair production, μ_{pair}, depends on the photon energy $h\nu$ and the atomic number Z of the material it passes through. Therefore, pair production is more likely to occur for high-energy photons in heavy materials:

$$\mu_{pair} \propto Z \ln(h\nu)$$

The Rayleigh scattering is an elastic scattering process in which the incident photon undergoes a change in direction, but no transfer of energy takes place. It is therefore a non-ionizing

process, but it contributes to diffusing the ionization throughout the material. For high energy radiation, as it is the case for space radiation, the phenomenon becomes negligible. The probability of occurrence is proportional to the atomic number of the material and inversely proportional to the photon energy:

$$\mu_{Compton} \propto \frac{Z^2}{(h\nu)^2}$$

Photonuclear reactions occur when high-energy gamma rays are absorbed by atomic nuclei, causing the nucleus to transition from an excited state to a lower energy state and emitting subatomic particles in the process. While most photonuclear reactions occur at photon energies rarely found naturally on earth, they can occur in space where the energies can go up to ~2.5 GeV. The summary of the possible photon interactions and their predominance are illustrated in Fig. 3a, 3b and 3c.

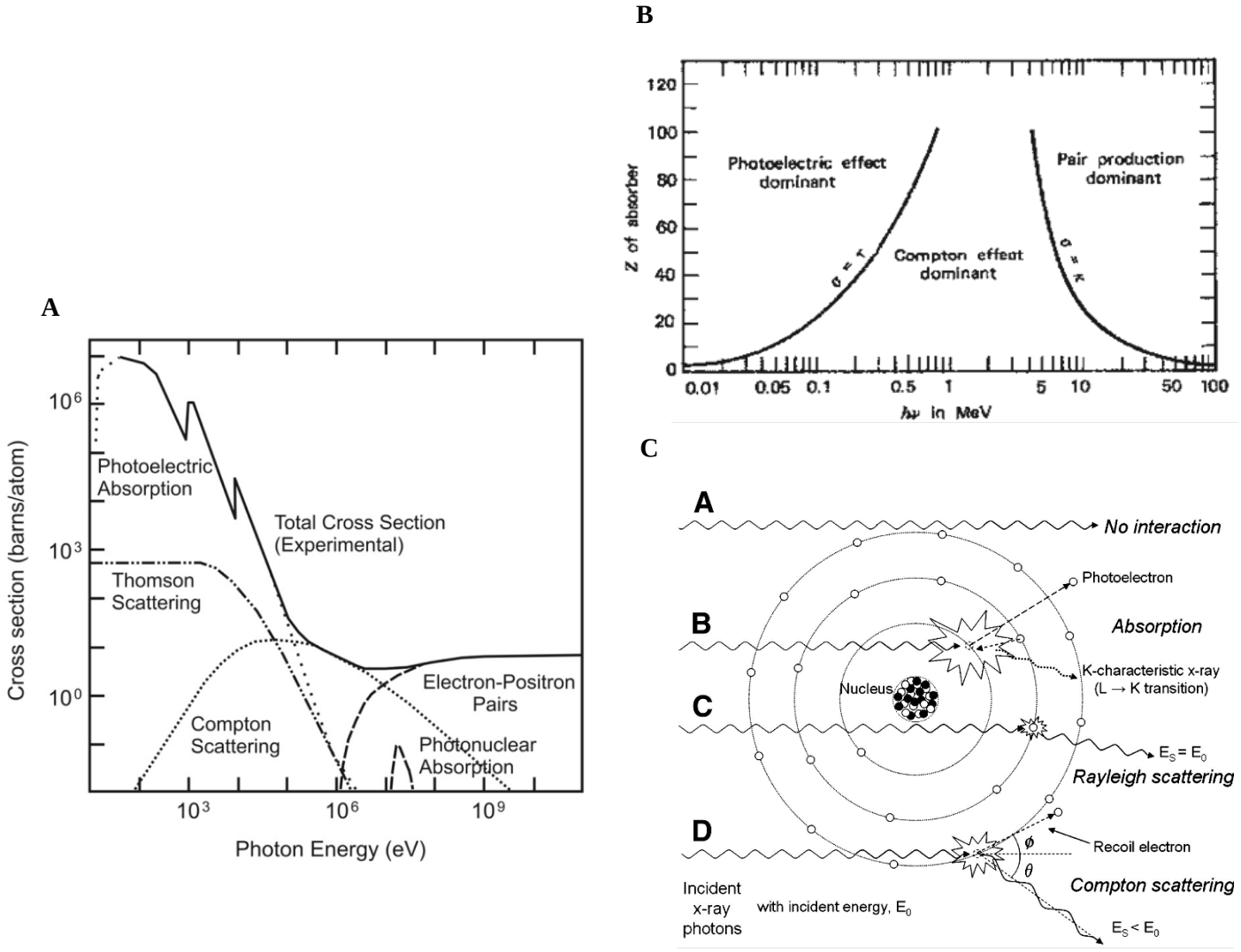

Fig. 3 Fig 3a displays in detail the superposition of the cross sections according to the photon energy (Gruber 2014). Fig 3b pinpoints the predominant ionizing process depending on the photon energy and the atomic number of the material (Almahwasi 2016). Fig 3c represents the possible interactions with an atom, without photonuclear processes (Seibert et Boone 2005).

Neutrons are electrically neutral, indirectly ionizing radiation that interacts only with nuclei. At high-energy, neutrons are diffused elastically or inelastically through matter via strong nuclear forces. In elastic diffusion, the neutron loses some of its energy to the nucleus through recoil, while in inelastic diffusion, the nucleus is excited and emits gamma rays. As neutrons slow down and reach thermal energies around 0.025 eV, they can be absorbed by nuclei through various nuclear reactions, including neutron capture or nuclear fission. The absorption probability and products depend on the material. For instance, the $^1H(n,\gamma)^2H$ reaction will emit gammas, whereas the $^3H(n,p)^3H$ reaction will emit a proton and the uranium fission will produce neutrons, ^{92}Kr and ^{141}Ba.

Directly ionizing radiation is characterized by charged particles that can interact with the nuclei or electrons of matter through Coulomb interaction, primarily with electrons due to their greater abundance. The energy loss of massive particles with atomic number z and speed v in a material of atomic number Z and density ρ is expressed in terms of the stopping power of the particle in matter, $-\frac{1}{\rho}\frac{dE}{dx}$. This stopping power is calculated using the Bethe-Bloch formula, which integrates the electromagnetic interaction between a relativistic charged particle and the electrons and nuclei of the target material:

$$-\frac{1}{\rho}\frac{dE}{dx} = \frac{N_A z}{A}\left[\frac{4\pi Z^2\alpha^2(\hbar c)^2}{m_e v^2}\right]\left[\ln\left(\frac{2m_e c^2\beta^2}{I(1-\beta^2)}\right) - \beta^2 - \frac{\delta}{2} - \frac{C}{z}\right]$$

With ρ the traversed material density, N_A the Avogadro number, A the mass number of the traversed material, $\alpha = \frac{e^2}{4\pi\varepsilon_0\hbar c}$ the fine-structure constant, $\hbar = \frac{h}{2\pi}$ the reduced Planck constant, $c \approx 3\times10^8\, m\cdot s^{-1}$ the speed of light, $m_e \approx 511\, keV/c^2$ the electron mass, $\beta = \frac{v}{c}$ and I the ionization constant, that considers the possible levels of excitation and their probabilities. It is given by:

$$\frac{I}{Z} = 9.76 + 58.8\cdot Z^{-1.2}\, eV \text{ for } Z \geq 13 \text{ and } \frac{I}{Z} = 12 + \frac{7}{Z}\, eV \text{ for } Z < 13$$

$-\frac{C}{z}$ and $-\frac{\delta}{2}(\delta \geq 0)$ are the screening and shell corrections for lesser energy particles. The screening correction accounts that the electromagnetic field of a positively charged incident particle as perceived by far electron is partially screened by the nearer electrons. The shell correction term corrects the assumption that the ion velocity is much larger than the target electron velocity. The term is usually calculated by detailed accounting of the particle's interaction with each electronic orbit in various elements and can contribute up to a 6% correction to stopping powers (Ziegler 1999). The Bethe-Bloch formula is the most accurate for particles in the MeV range to a few hundred of GeV. It states that a particle's speed decreases as it passes through matter, resulting in an increased stopping power of the material. Consequently, there is a maximum energy loss of the particle just before it comes to a stop, known as the Bragg peak. Light particles like electrons experience constant changes in their trajectory when colliding with matter, leading to a shallow penetration depth. On the other hand, ionizing particles from the periodic table continue their path in a straight line with a minor diffusion caused by electron scattering. This slight deflection is known as straggling. The penetration depth, and dose deposition patterns can be compared in Fig. 4a.

Lighter particles, such as electrons and positrons, interact with matter through two distinct processes. First, they undergo ionization and excitation like the heavier particles, but in addition, they also experience the Bremsstrahlung process. Bremsstrahlung radiation is continuous and occurs when a charged particle decelerates in the electric field of a nucleus, resulting in the emission of photons. This process is particularly significant for light particles because its probability to produce a photon of energy E_γ is inversely proportional to the mass of the particle m and directly proportional to the atomic number Z of the material it traverses:

$$\frac{d\sigma}{dE_\gamma} \propto \frac{Z^2}{m}\frac{1}{E_\gamma}$$

The ratio of the radiative and collisional stopping powers of the electron is approximately:

$$\frac{(dE/dx)_{rad}}{(dE/dx)_{coll}} \approx \frac{Z\,E(MeV)}{560}$$

The collisional stopping power is predominant until a critical energy above which the energy is mainly lost through Bremsstrahlung. Fig. 4b illustrates the stopping power of electrons in Cu. The critical energy above which the radiative contribution is predominant is around 20 MeV.

A

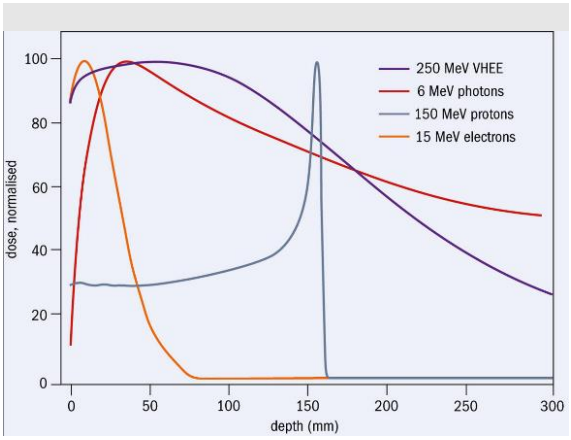

B

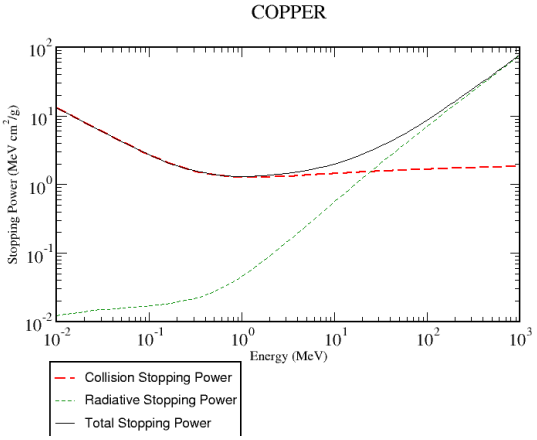

Fig. 4 Fig. 4a represents the deposition of energy (normalized dose) for 15 MeV electrons, 6 MeV photons, 150 MeV protons and 250 MeV electrons (« Very High-Energy Electrons for Cancer Therapy » 2020). We can see that for reasonable energy, the penetration depth of the electrons is very small whereas the proton deposits most of its energy at the Bragg peak. Photons deposit their energy in an exponentially decreasing fashion. Fig. 4b represents the stopping power of electrons in copper (« estar-stopping power and range tables for electrons » 2023). The transition between collisional and radiative stopping power is around 10 MeV.

The Linear Energy Transfer or LET is a measure of the amount of energy that is deposited locally by an ionizing particle per unit length of its path through a material. In other words, LET describes how much energy a particle transfers to the material it passes through, per unit length. The higher the LET of a particle, the more energy it deposits in the material per unit length, which means it can cause more damage to the biological tissue it interacts with. It is generally expressed in $keV/\mu m$ and can be approximated by:

$$LET\ (keV/\mu m) = \frac{dE}{dx}$$

with $\frac{dE}{dx}$ the stopping power. The LET is a local variable that excludes the secondary particles that move away from their production site. Low LET radiation refers to ionizing radiation that has a low linear energy transfer, meaning it deposits relatively small amounts of energy per unit length of its path through a material. Examples of low LET radiation include gamma rays and X-rays. High LET radiation, on the other hand, refers to ionizing radiation that has a high linear energy transfer, meaning it deposits a large amount of energy per unit length of its path through a material. Examples of high LET radiation include alpha particles, beta particles, and heavy ions. High LET radiation is typically more damaging to biological tissue than low LET radiation, as it can cause more DNA damage in the cells it interacts with.

Ionization effects on living organisms and radiation quantification

Absorbed dose, evaluated in Gray (Gy), quantifies the amount of energy deposited by ionizing radiation in a material per unit mass. However, for assessing the biological effects of radiation, the concept of equivalent dose is used, which considers the radiation type, energy, and the sensitivity of different tissues to radiation damage. In other words, equivalent dose measures the biological effect of radiation on the body (Penninckx 2023). However, in this specific study, where the focus is on both investigating the physical and biological implications of radiation, the absorbed dose in Gray provides a more straightforward and versatile unit for quantifying the energy deposition from radiation.

When ionizing radiation passes through a cell, it can cause damage to many components. However, the most significant and harmful damage occurs in the DNA of the traversed cells. The damage to the DNA can be either direct or indirect. In direct damage, the ionizing radiation reaches the DNA and ionizes it. In indirect damage, the ionizing radiation can initiate a chain reaction that can propagate in the cell and damage the DNA. The quantity of damage to the DNA, whether direct or indirect, depends on the dose delivered, the type of radiation, and its energy. For the same initial energy, high linear energy transfer (LET) radiation creates more ionizations and, therefore, more damage. The types of DNA damage include simple DNA strand breaks (SSBs), double-strand breaks (DSBs), and base damage. For most living animals, if there is too much damage to the DNA, the cell dies. However, most animals have cellular repair mechanisms for DNA that can repair the initial structure to some extent, sometimes leading to mutations in the DNA code. The repair mechanisms for *Adineta vaga* are not fully understood, but they are thought to play a significant role in their extreme resistance to radiation.

Geant4

Geant4 is a powerful simulation toolkit written in C++ that utilizes statistical Monte Carlo methods to simulate the global behavior of particles passing through matter (Agostinelli et al. 2003; Allison et al. 2006; 2016). The Monte Carlo method models the behavior of each particle individually by selecting a random interaction among all possible interactions at each step (« Geant4 Documentation » 2023). The simulation starts with the particle's initial conditions, such as its energy and direction. Using a transportation module, the simulation computes the

free path before the next interaction to determine where the particle will be at the next step. At each step, the simulation calculates the probability of various interactions based on empirical or theoretical physical models and selects one randomly. This process continues until the particle either stops or exits the simulation volume. By simulating numerous particles, Geant4 can reproduce global quantities such as energy deposition. To avoid unreasonable computation time, Geant4 provides a set of physics lists, which are sets of physical interactions that specialize for a given study case, such as an energy range or a specific physical process like hadron collisions. The physics lists are designed to be more precise and complete in their specialization and less precise elsewhere.

The particle transport is performed step by step. At each step, the length of the step is either determined by the mean free path of the randomly selected interaction event or a step limitation, such as crossing a boundary between two materials. To calculate the mean free path of a particle in each medium, Geant4 employs the cross-section of a specific physics process listed in the physics list and the density of atoms in the material. This calculation helps to determine the probability of the particle undergoing an interaction with the medium. In a compound material, the number of atoms per volume can be calculated using the formula $n_i = \mathcal{N}\rho\omega_i/A_i$, where $\mathcal{N}$ is Avogadro's number, ρ the density of the material, ω_i the mass proportion of the i^{th} element, and A_i is the mass of a mole of the i^{th} element. The mean free path of a process λ can thus be given in terms of the total cross section:

$$\lambda(E) = (\sum_i [n_i \cdot \sigma(Z_i, E)])^{-1}$$

With $\sigma_{i(Z,E)}$ the total cross section per atom of the process. The sum runs over all elements composing the material. The cross sections per atom and mean free path values are mostly tabulated during initialization.

As an example, let us consider the photoelectric effect for gammas. The cross section of the photoabsorption is parametrized to determine the mean free path. The parametrization of the photoabsorption cross section is used with the approximation:

$$\sigma(Z, E_\gamma) = \frac{a(Z, E_\gamma)}{E_\gamma} + \frac{b(Z, E_\gamma)}{E_\gamma^2} + \frac{c(Z, E_\gamma)}{E_\gamma^3} + \frac{d(Z, E_\gamma)}{E_\gamma^4}$$

That uses a least-square method on *a*, *b*,*c* and *d* to fit experimental data.

The following section is an article currently undergoing review for publication in Hydrobiologia. The study utilizes Topas, a user-friendly interface of Geant4, to examine the radiation coverage of bdelloids in three experimental setups. The aim is to establish a correlation between the output of simulation radiation coverage and fertility data and compare the coverage patterns of radiation of different nature.

Section 2: Hydrobiologia article

A. vaga Under Fire: Simulating the Impact of Radiation

Alexandre Perrot [1], Boris Hespeels [2,3], Karine Van Doninck [2,4], A-C. Heuskin [1*]

[1] Laboratory of Analysis by Nuclear Reactions (LARN), Namur Research Institute for Life Sciences (Narilis), University of Namur, Namur, Belgium.

[2] Research Unit in Environmental and Evolutionary Biology (URBE), Laboratory of Evolutionary Genetics and Ecology (LEGE), NAmur Research Institute for Life Sciences (NARILIS), University of Namur, Namur, Belgium.

[3] Research Unit in Environmental and Evolutionary Biology (URBE), Institute of Life, Earth & Environment (ILEE), University of Namur, Namur, Belgium.

[4] Research Unit in Molecular Biology and Evolution, DBO, Université libre de Bruxelles (ULB), Brussels 1050, Belgium.

* Corresponding author

E-mail: anne-catherine.heuskin@unamur.be

Keywords: Extreme Tolerance; Bdelloid Rotifers; Simulation; Ionizing Radiation; Topas; Low and high LET

Abstract

Previous studies have demonstrated the remarkable resistance of bdelloid rotifers to ionizing radiation, making them an interesting model for studying radiation effects on living organisms. This study investigates whether radiation exposure, as performed in previous studies, affects all bdelloids equally and explores the relationship between biological data and energy deposition patterns induced by low and high linear energy transfer (LET) radiation, using proton, iron ion, and X-ray simulations. The simulations showed that all individuals, cells, and nuclei were effectively hit by the administered doses of 4 MeV protons, 0.5 GeV/n 56-Fe, and X-ray radiation. The results support that survival and fertility rate impacts are due to radiation-induced

damage rather than the absence of hits in certain individuals or germinal cells. Notably, simulations revealed significant differences between low and high LET radiation concerning irradiated individuals' nuclei, highlighting the sparse and diffuse distribution of radiation hits for high and low LET radiation, respectively. In conclusion, the study supports the idea that reduced fertility described in high LET-exposed samples is associated with complex DNA damage caused by the condensed energy deposition pattern of high-LET radiation compared to low LET.

Introduction

With a worldwide distribution, bdelloids are among the tiniest metazoan on the planet. One remarkable feature of bdelloid rotifers, being even more unusual among animals, is the absence of males, vestigial male structures, or hermaphrodites in any of the populations studied within the 460 described morphospecies. Bdelloid rotifers are females apparently cloning themselves since millions of years (Maynard Smith 1986; Judson et Normark 1996; Segers 2007). Approximately 90% of bdelloid species have been documented to inhabit semi-terrestrial habitats such as mosses and lichens (C. N. Ricci 1987; C. Ricci 2017; Melone et Fontaneto 2005). These habitats are known for sudden and sometimes rapid changes in physical and chemical conditions like temperature, food, chemical composition, and water availability. Adapted to temporary environments, most, but not all, bdelloids are able to enter and survive desiccation at any stage of their life cycle and resume reproduction after rehydration without negative effects. The desiccation resistance was shared with other small animals associated with limno-terrestrial environment like some nematodes and several tardigrade species (C. Ricci et Pagani 1997; Rebecchi et al. 2006). It remains however unclear how desiccation resistant organisms deal with this unpredicted decrease in water content, a process that induces cellular damages (*e.g.*, protein aggregation and denaturation), DNA damages, leakage of cellular membranes and generation of reactive oxygen species (ROS) (M. Potts 1994, 94; Mattimore et Battista 1996; Shirkey et al. 2003; Alpert 2005; Gusev et al. 2010; Crowe 2014; Hespeels et al. 2014). Moreover, in order to remain viable, dried organisms must acquire mechanisms that maintain the function of their macromolecules (*e.g.*, proteins, DNA) and membranes, and the capacity to restart their metabolism when water becomes available (Malcolm Potts et al. 2005; Leprince et Buitink 2015).

The notorious desiccation tolerance of bdelloid rotifers seems to provide them with a high tolerance to a variety of stresses including high pressure, vacuum, UV or freezing (C. Ricci et al. 2005; Fischer et al. 2013). In 2008, Gladyshev and Meselson demonstrated for the first time that two bdelloid rotifer species are extraordinarily resistant to ionizing radiation (IR) (E. Gladyshev et Meselson 2008). Exposure of cells to ionizing radiation triggers a complex chain of physical, chemical, and biological processes, varying in terms of timing, spatial distribution, and energy scale, making the cellular response challenging to predict (Joiner et van der Kogel 2018). The ionization density in particle tracks is typically characterized by Linear Energy Transfer (LET), which refers to the average energy (in keV) deposited by a charged particle per unit distance traveled (1 μm). High-Z charged particles, such as Fe ions, are considered high LET due to their high ionization density along their path, while photons, such as X-rays, produce sparse ionizations and are therefore considered low LET ionizing radiation (Joiner et van der Kogel 2018; Hagiwara et al. 2019). While the same radiation dose produces a similar

quantity of ionizations, the differences in their spatial distribution result in diverse biological damages. It has been shown that low LET radiation, with their sparse ionizations, primarily cause DNA base oxidation and single-stranded breaks (Lehnert 2007). In contrast, exposure to high-LET radiation leads to the formation of complex DNA damages, including clustered double-stranded breaks (DSBs), which results in a reduced survival of the irradiated organisms (Semenenko et Stewart 2004). To document the energy deposited by ionizing radiation in the matter or cell, the absorbed dose is expressed in Gray (Gy). Mathematically, it was defined as the ratio of the energy deposited by the radiation to the mass of the matter traversed.

Desiccated *A. vaga* individuals were able to survive doses higher than 5000 Gy of X-ray and proton radiation, which was striking compared to the Lethal Dose 50 (i.e., the dose required to kill 50% of the irradiated population) of mammalian cells, which ranges from 2 to 6 Gy after X-ray exposure. Other studies have demonstrated the resistance of different bdelloid species to various types of radiation. For instance, *Mniobia russeola* has been found to withstand heavy ions such as iron (Fe) and helium (He), while *Philodina roseola* exhibits high resistance against gamma radiation (E. Gladyshev et Meselson 2008; Jönsson et Wojcik 2017). This radioresistance may appear obscure since none of the exposed radioresistant species were ever confronted with such levels of radiation in their natural environment. By analogy with the extreme desiccation and radiation resistance of the bacterium *Deinococcus radiodurans* (Mattimore et Battista 1996), it has been hypothesized that the extraordinary radiation resistance of bdelloid rotifers reflects an adaptation to their desiccation resistance (E. Gladyshev et Meselson 2008; E. A. Gladyshev et Arkhipova 2010). Indeed, the extreme radiation resistance of *D. radiodurans,* surviving gamma radiation doses higher than 20.000 Gy, was attributed to their ability to deal with massive amount of DNA DSB accumulated during desiccation. Indeed, a similar impact on genomic integrity was recorded in samples of *D. radiodurans* desiccated for 6 weeks or irradiated with 5.200 Gy of gamma radiation. Secondly, *D. radiodurans* was able to restore genomic integrity post rehydration or irradiation (Mattimore et Battista 1996). Similarly, it has been demonstrated that prolonged desiccation or exposure to high dose of IR generates hundreds of DNA DSB in nuclei of bdelloids that are fully or partially repaired post rehydration or irradiation (Hespeels et al. 2014; 2020). Indeed, *A. vaga* individuals were able to restore the genomic integrity of their germinal cells after high dose to IR (>500 Gy) (Terwagne et al. 2022). On the other hand, an incomplete DNA DSB repair was observed in their somatic cells suggesting that genetic alterations at the sequence level may be tolerated in somatic cells due to their non-cycling, postmitotic status or the absence of signaling for unrepaired DNA DSBs, which often triggers apoptosis (Hespeels et al. 2020; Terwagne et al. 2022).

The radio-resistance of *A. vaga* individuals was differentially interpreted, in term of magnitude, when focusing on the survival rate or on their capacity to produce viable offspring. In a previous study, we reported a factor of approximately 3 between doses required to sterilize a population or to kill all exposed animals. Indeed, the median sterilizing doses (SD50) for the *A. vaga* individuals were 1,035 ± 20 Gy, 453 ± 23 Gy and 461 ± 1 Gy for X-ray, protons and iron, radiation exposure respectively. A 2.3 factor was reported when comparing SD50 of X-ray versus protons and Fe particles. Indeed, it would have taken twice as much dose deposited in the case of X-rays to sterilize individuals in comparison with protons and iron particles (Hespeels et al. 2020). These observations, also reported for tardigrades exposed to IR, were hypothesized to be attributed to the nature of the cells evaluated through survival or fecundity rate assays. The survival rate in those metazoans is related to non-dividing somatic cells, while

fertility data is linked to germinal cells that will ensure cellular multiplication during embryonic development and as consequence are more sensitive to damages induced by radiation (Pagani, Ricci, et Redi 1993; Beltrán-Pardo et al. 2015). The precise causes of these differences remain to be investigated but may be informative to the documentation of damage type induced by low and high LET radiation on a radioresistant metazoan.

Until recently, DNA damage quantification of irradiated bdelloid individuals relied mainly on the semi quantitative approach PFGE (Pulsed Field Gel Electrophoresis). However, this technique was not able to provide information related to each type of cell and was biased toward damage affecting somatic cell of bdelloids (E. Gladyshev et Meselson 2008; Hespeels et al. 2014; 2020). In a new study, Terwagne et al., reported, using TUNEL assay approach, the presence of DNA DSB in primary oocyte of *A. vaga* individuals exposed to the sterilization dose of 1280 Gy of proton radiation (Terwagne et al. 2022). As a matter of fact, it remains plausible that the fertility curve reported previously may be affected by the presence of untargeted animals or germinal cells during irradiation.

In this study, TOPAS, a simulation tool based on Geant4 (Agostinelli et al. 2003; Allison et al. 2006; Perl et al. 2012; Faddegon et al. 2020), is used to reevaluate how radiation sources previously used against *A. vaga* individuals target and hit these individuals at population and individuals specific level (Hespeels et al. 2020). In other terms, we sought to determine which fraction of individuals and cells are effectively targeted by radiation. These data are critical to ensure a good comprehension of bdelloid radiation data and exclude the possibility that the radiation resistance may be linked with untargeted individuals/cell types. Finally, we compared simulation data of low and high LET radiation and discussed these data with previously published data.

Materials and Methods

Topas and modeling of bdelloid samples

The software used is TopasMC, version 3.7. Topas is an extension of Geant4, a Monte Carlo simulation software, designed for the transport and interactions of charged and uncharged particles in matter (Agostinelli et al. 2003; Allison et al. 2006; Perl et al. 2012; Faddegon et al. 2020). Whole sets of electromagnetic, hadronic, and optic processes called physics lists can be simulated over a wide range of particles and energies. The Livermore list is chosen as it is specialized in weak energy interactions, from 100 GeV down to 250 eV.

The next step involves defining the geometry, materials, and radiation sources. Three levels of granularity were utilized to replicate experimental setups from previous research (Hespeels et al. 2020). At the first level, a layer of desiccated bdelloids is modeled and subjected to irradiation to determine the dose distribution across individual bdelloids. Fig. 1 compares a TEM image of the layer and the modeled geometry. At the second level, a single desiccated bdelloid is modeled and exposed to radiation to determine the dose distribution across all its nuclei. To provide a detailed view of the bdelloid patch, Fig. 1 displays a close-up TEM image, where the outline of a single bdelloid is highlighted in red.

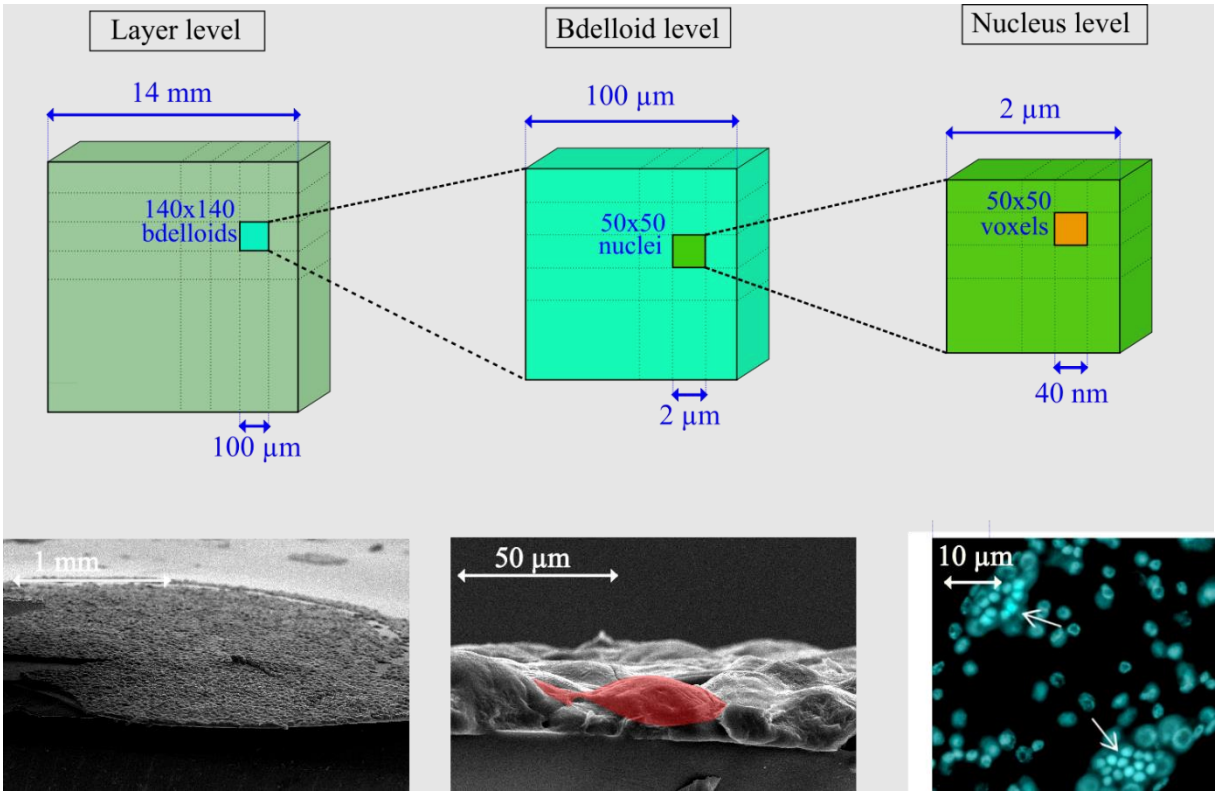

Fig. 1 View of the three modeled levels of granularity simulated in Topas: monolayer of desiccated bdelloid, bdelloid individual and nucleus level. The modeling is based on TEM reference images. The layer level is a 14x14 mm^2 large and 30 µm thick cube, as the TEM layer is roughly circular, with a 14 mm diameter and 30 µm thickness on average. It is divided into 140x140 bdelloid voxels that correspond to the desiccated individuals. The bdelloid is 100x100 $µm^2$ large and 30 µm thick, from the dimensions of a bdelloid individual highlighted in red on the TEM image. It is subdivided into 50x50 nuclei voxels. The nucleus level is 2x2 $µm^2$ large, 30 µm deep and divided into 50x50 voxels to provide a DNA level resolution of damage location. The third level confocal imagery shows somatic and germinal cells of hydrated *A. vaga* individuals. Nuclei were counterstained with DAPI (blue). Arrows indicate the pools of primary oocytes. Scale bar: 10 µm. Picture from (Terwagne et al. 2022)

Bdelloid layers are aggregates of desiccated bdelloids as used in (Hespeels et al. 2020). Experimentally, the desiccation process takes place on an agarose support of approximately 100 µm thickness. A bdelloid layer has on average a 14 mm diameter and 30 µm thickness (based on the TEM images as in Fig. 1). The thickness is subject to biological variability such as impurities or overlap of bdelloid individuals. Bdelloid layer is nevertheless modeled as a cube of 14x14 mm^2 with 30 µm thickness. Indeed, a cube can be segmented into cubic volumes. Thus, the layer can be segmented in 140x140 voxels of 100x100 $µm^2$. This corresponds roughly to the dimensions of a desiccated bdelloid (Terwagne et al. 2022). Similarly, for the second level of simulation, a single bdelloid of 100x100 $µm^2$ surface is segmented in 50x50 voxels of 2x2 $µm^2$, which corresponds to the order of magnitude of a nucleus surface (Terwagne et al. 2022), thus enabling nuclei level resolution. The third level models a single nucleus with 2x2 $µm^2$ surface. It is segmented in 50x50 voxels of 40x40 nm, which is convenient to investigate damage repartition at the nucleus level. Topas uses user-defined materials. The exact composition of bdelloids is unknown, but the chemical composition of human skin (H10C20N4O65S0.2Cl.3Na.2K.1) was selected as giving the best approximations of the experimental LET.

Experimental setups and modeled geometries

The geometries modeled in Topas accurately replicate the experimental setups used in reference (Hespeels et al. 2020). All geometry elements are contained in a 1x1x1 m^3 virtual cube of vacuum called *world*. The world cube is a computational boundary beyond which physical processes are not simulated. Three experimental setups are modeled: 4 MeV protons, 0.5 GeV/n ^{56}Fe ions and X-rays irradiation.

4 MeV proton: A layer of bdelloids is irradiated by a 1 cm^2 beam of 4 MeV protons. The beam is produced in vacuum and extracted in air through a 1 µm Si_3N_4 window. It then travels through 3 mm of air to reach the bdelloid layer on its agarose support. The doses received by the layer ranged experimentally from 100 to 10,000 Gy (Hespeels et al. 2020). The surface of the beam is larger than the sample to provide uniform irradiation. Preliminary simulation has shown that the presence or absence of the agarose support (located after the bdelloid layer) has no impact on simulation outputs. No backscattered protons have been observed, and the contribution of backward emitted secondary electrons created within the agarose layer is negligible (data not shown). It has therefore been removed to speed up the calculations. The simulated geometry is represented on Fig. 2a.

*X-ray*s: In (Hespeels et al. 2020), bdelloids were irradiated with a X-Rad 225-XL (PXi, USA), with spectrum energy ranging from 10 to 225 keV. The desiccated samples received doses ranging from 100 to 7,500 Gy. The modeled geometry used for the X-ray is identical to the one used for proton exposure. The only difference is the source particles, changed from protons to gamma particles.

0.5 GeV/n ^{56}Fe ions: In (Hespeels et al. 2020), up to 20 layers of bdelloids were stacked in a plastic tube. Additional 100 µm agarose and 10 µm aluminum foil layers were placed in front of the bdelloids to hold them in place. The iron beam was wider than the sample to irradiate its surface uniformly. The system is modeled using squared plastic tube and layers for the sake of even surface subdivision. Heavy ions simulation can be computationally costly. Therefore, the following approximations are made. The beam is set just as wide as the system, to avoid simulating useless ions. Most importantly, the dose deposition is similar for all stacked layers. Preliminary simulations showed that the Bragg peak (i.e., the increase in LET due to the slow-down of the ions) occurs around 800 stacked bdelloid layers (data not shown). Therefore, a single layer of bdelloids is modeled. The simulated geometry is represented in Fig. 2b.

Sources: Particles sources are implemented in Topas as beams, with user-defined geometries. All simulations use a 14x14 mm^2 wide squared beam to cover the bdelloid layers. The sources are placed upstream, at the limit of the world cube. Particles are homogeneously distributed within the beam. The energy of proton and ^{56}Fe particle sources is unique: 4 MeV and 0.5 GeV/n respectively as used in (Hespeels et al. 2020). For X rays, the energy spectrum of a 225 kVp Comet MXR 161 XR tube as used in (Hespeels et al. 2020) is implemented using the *SpekCalc* software (G. G. Poludniowski 2007; G. G. Poludniowski et Evans 2007; G. Poludniowski et al. 2009). The output of SpekCalc is implemented in Topas using a custom python script. Particles sources of continuous energy are implemented in Topas as two vectors: one containing the energy values, and one containing their probability of occurrence (as normalized relative intensity). Topas being a MonteCarlo simulation software, it simulates each particle individually. The user sets a pre-defined number of particles to simulate.

Scoring: Dose, and other physical measurements, are retrieved with *scorer* elements. Three scorers are used: *DoseToMedium*, *SurfaceTrackCount* and *PhaseSpace*. The DoseToMedium scorer is assigned to a geometry element and computes the deposited dose in the volume. It can segment the geometry element to retrieve the dose in every voxel. This scorer can be used in all simulation levels to find the dose distribution over the bdelloid layer, the dose distribution over the nuclei of a single bdelloid or the dose repartition inside a nucleus. The SurfaceTrackCount scorer is assigned to a geometry element and delivers the number of particles crossing its surface. This scorer can also segment the geometry element in voxels and is used to retrieve the distribution of particles over the voxels. Finally, The PhaseSpace scorer is assigned to a surface. It stores information about the particles crossing its surface in an output file: X, Y and Z positions, momentum direction, type of particle, charge, energy in MeV, weight, Particle ID, a Boolean flag if the direction of cosine is negative and finally if the scored particle is a primary or secondary particle. A PhaseSpace can be used as source in another simulation. Here, the PhaseSpace is recorded at the first level of granularity (bdelloid layer) to save particles crossing one voxel, i.e., a single bdelloid. This PhaseSpace can then be used as a source in the single bdelloid level (second level of granularity) to study the dose repartition over its nuclei. Fig. 2c illustrates this principle, which is less resource consuming than scoring both levels of granularity in one simulation. Simulations on a full layer and on a single bdelloid level were conducted for the three types of particle sources described above.

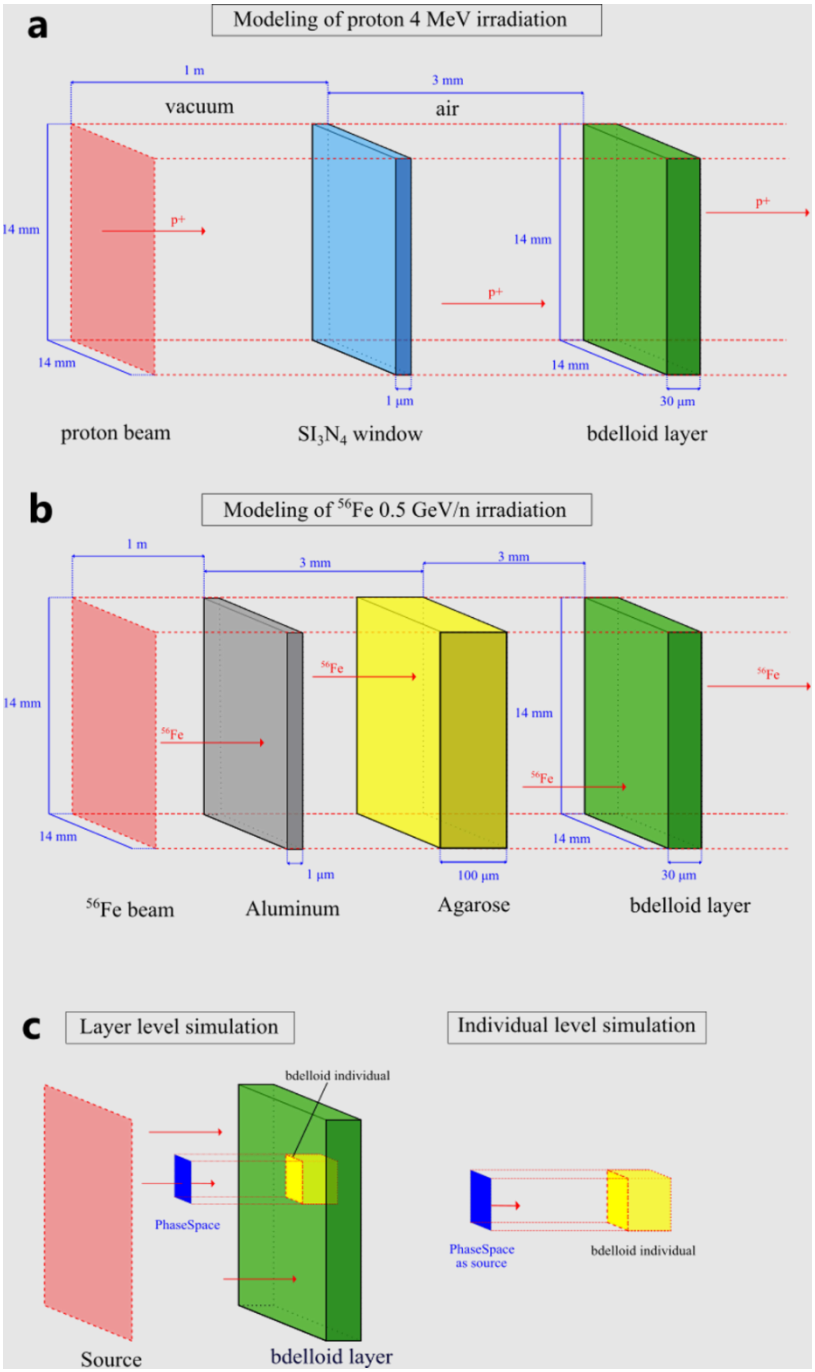

Fig. 2 Proton (a) and ^{56}Fe (b) irradiation setups and PhaseSpace scorer (c). Fig. 2a depicts the proton irradiation setup. A 14x14 mm proton beam is placed in vacuum, 1 meter away from the setup. Protons are extracted from the vacuum through a 1 µm thick window of Si_3N_4. After traversing 3 mm of air, the protons reach the bdelloid layer. This setup is identical for X-ray, with the only difference being the type of particle used. In Fig. 2b, a 14x14 mm^2 ^{56}Fe beam is placed in air, 1 m ahead of the setup. The beam passes through a 1 µm thick layer of aluminum before crossing 3 mm of air and reaching a 100 µm agarose layer. After another 3 mm air, it reaches the bdelloid layer. In the simulation, the setup (aluminum, agarose and bdelloid layer) is placed in a PCR tube. However, the latter is not drawn to ease the reading of the figure. Fig. 2c illustrates the use of the PhaseSpace scorer. During the layer-level simulation (left), a virtual surface with no interactive properties is created upstream of the selected bdelloid voxel. The scorer is attached to this surface and registers all particles that pass through it. The scorer can be used as source in subsequent simulations to irradiate a unique bdelloid (right). The figures are not drawn to scale for ease of reading.

Poisson distribution as a tool to describe the spatial repartition of particles

Modeling bdelloid layers as cubes is convenient, as cubes are easily subdivided into voxels of identical surfaces. As described before, a 14x14 mm bdelloid layer surface can be subdivided in voxels of 0.1x0.1 mm², i.e., the dimensions of a single bdelloid. By associating a DoseToMedium scorer to each voxel, the dose distribution over the bdelloids can be retrieved. For high doses (i.e., high number of particles) and for a uniform beam, the distribution follows a normal law, but for lower doses (less particles), the distribution is more adequately described by the Poisson distribution. The Poisson distribution is a discrete probability distribution, defined by a single parameter $\mu \in \mathbb{R}$. Its probability mass function formula is the following:

$$\mathrm{P}(X = k) = \frac{\mu^k e^{-\mu}}{k\,!}$$

With P(X=k) the probability to measure X of valor k and μ the mean value of the distribution. Because X is discrete, it cannot directly represent the dose, which is continuous. The latter, fortunately, is proportional to the total number of particles. Thus, scoring with SurfaceTrackCount on every bdelloid provides the spatial Poisson distribution of the particles. In this case, P(X=k) is the probability for a bdelloid to be traversed by k particles. μ represents the mean number of particles passing through a bdelloid, which can be related to the mean dose over the bdelloid layer.

The Poisson description was used on the second level of granularity as well. By subdividing a 100x100 µm² bdelloid surface in 50x50 voxels corresponding to 2x2 µm² nuclei, the Poisson distribution can describe the spatial repartition of the particles over the nuclei. P(X=k) represents here the probability for a nucleus to be traversed by k particles. μ represents the mean number of particles passing through a nucleus, related to the mean dose over the single bdelloid. The exact proportionality relation is, for particles, the broad beam formula:

$$D = \frac{1.6 \times 10^{-9} LET\phi}{\rho}$$

With D the dose (in Gy), LET the linear energy transfer of the particle, ϕ the fluence (in particles/cm^2) and ρ the density of the target environment (in g/cm³). As $\mu = \frac{N_{tot}}{N_{voxels}}$, the ratio between the total number of particles and the number of voxels, for a given total number of particles, it is possible to relate µ and the expected dose output through the beam fluence. The key advantage of the Poisson description is that it can be used on every level of simulation: either to describe the repartition of particles over the nuclei of a bdelloid or the repartition of particles over the individuals composing a layer. The only difference will be in the values of N_{voxels} = 19,600 for bdelloid voxels and 2,500 for nuclei voxels.

Results

We aimed to investigate whether radiation exposure could lead to partial or complete sparing of certain bdelloids, or whether every nucleus of every bdelloid would be impacted as the radiation dose increased. Additionally, using simulations, we investigated whether biological data could be associated with specific energy deposition patterns at DNA level induced by low

and high LET radiation. To evaluate the validity of these hypotheses, we modeled all three radiation qualities (i.e., protons, iron ions, and X-rays) previously applied on desiccated bdelloids in (Hespeels et al. 2020).

Simulation of desiccated bdelloids exposed to proton beam

The first aim was to determine the minimal dose required on a layer to damage all nuclei of the bdelloids contained within. Since the dose on a layer is the average of the dose over its constituent bdelloids, there will be a bdelloid dose distribution centered on the layer dose. The least damaged bdelloids are expected to be located at the lower end of the distribution and are more likely to remain unaffected at the individual or germinal cells level. Therefore, the initial step in this investigation was to establish the minimal dose required to damage all germinal cells of the least damaged bdelloids in the layer. First, a single bdelloid was modeled and exposed to an increasing number of incident 4 MeV proton particles. The *A. vaga* individual is virtually divided into 50x50 nuclei voxels (2x2 μm^2 each). The dose for each voxel is obtained using the DoseToMedium scorer.

Fig. 3a illustrates the dose distribution across the nuclei in the bdelloid model. Before a total of $23x10^3$ particles, some nuclei receive a dose of 0 Gy, indicating that a cell can remain undamaged. For example, at $2x10^3$ particles (the blue curve in Fig. 3a), 45% of the nuclei score a null dose. At $12x10^3$ particles, (the orange curve in Fig. 3a), 0.64% of the nuclei score a null dose. From $23x10^3$ particles onwards (green curve in Fig. 3a), every single nucleus of the bdelloid is damaged and the corresponding dose distribution in nuclei ranges from 0.30 Gy to 7.14 Gy. On average, the dose delivered to a bdelloid is 2.99 Gy. Therefore, based on our modeling results, a minimal dose of 2.99 Gy is required to damage every nucleus in desiccated bdelloid individuals using 4 MeV protons.

The second simulation output is obtained by maintaining the same geometry and employing the SurfaceTrackCount scorer to count particles crossing each nucleus's surface. Fig. 3b presents the particle distribution for an increasing number of incident particles. Regarding the dose distribution, at $2x10^3$ particles (blue curve in Fig. 3b), 45% of voxels register 0 particles, with a mean value per voxel of 0.80 particles. At $12x10^3$ particles (orange curve in Fig. 3b), 0.64% of voxels register 0 particles with a mean value per voxel of 5.2 particles, and at $23x10^3$ particles (green curve in Fig. 3b), all voxels register between 1 and 22 particles, with a mean value $\mu=9.2$ particles. The 45%, 0.64%, and 0% proportions of untouched voxels remain consistent for both dose and particle distributions. Since protons continuously interact with matter, a particle passing through a voxel is guaranteed to deposit energy. Overall, this simulation level indicates that $23x10^3$ incoming protons will deposit 2.99 Gy in a single rotifer, and damage all its nuclei. The Poisson description adequately describes the particle count distribution and indicates that all the nuclei are hit by 9 particles on average at this threshold dose (see Fig. 3b). To simulate at the rotifer layer level, a minimum particle count per rotifer of $23x10^3$ will ensure that no rotifer or nucleus is spared by radiation. To account for the width of the Poisson distribution and push threshold-irradiated individuals to the lower end of the dose distribution, the total dose delivered to the full layer should be superior to 2.99 Gy. For instance, using $\mu=23.7x10^3$ (as mean particle count per voxel, corresponding to 3 Gy) at the layer level satisfies to the previous requirement.

In the third part of the simulation, a layer of desiccated bdelloids measuring 14x14 mm^2 is modeled. The layer is further divided into 0.1x0.1 mm^2 individual bdelloids, resulting in

140x140 bdelloid voxels in total. This simulation aims to demonstrate the variability of exposure across the population of bdelloids in a layer. A mean dose of 6.54 Gy was delivered, which ensures that the 3 Gy threshold determined above is exceeded. The results are presented in Fig. 3c and 3d. Histogram c in Fig. 3 illustrates the dose distribution across the bdelloids in the layer, ranging from 6.42 Gy to 6.65 Gy. As expected, no bdelloid scores 0 Gy at the individual or nucleus level. To further highlight the dose disparities, we assign three PhaseSpace scorers to three different bdelloids, which are highlighted on histogram c: a bdelloid that receives a lower dose (irradiated at 6.46 Gy, shown in blue in histograms c and d), an average irradiated bdelloid (irradiated at 6.54 Gy, shown in green in histograms c and d), and a highly irradiated bdelloid (irradiated at 6.62 Gy, shown in red in histograms c and d). Fig. 3e illustrates in a different way the dose repartition over the average irradiated bdelloid using a color map. The doses range from 1.95 to 11.97 Gy, but no nucleus scored 0 Gy.

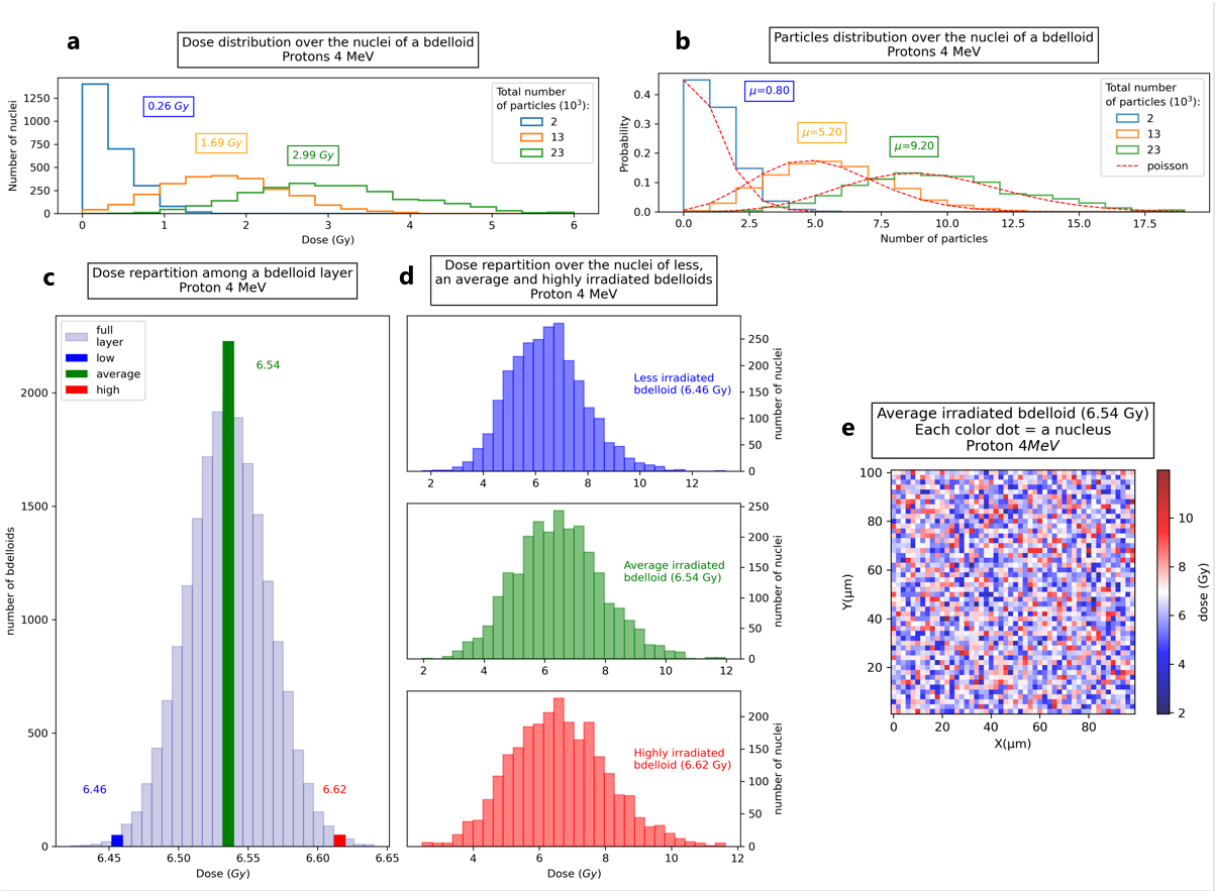

Fig. 3 Analysis of Dose Distribution, Particle Count, and Irradiation Variability in bdelloid model exposed to Proton 4 MeV. Fig. 3a presents the dose distribution for three different total particle counts. The histograms, represented in blue, orange and green, count the number of nuclei that have received a given dose. Fig. 3b presents the particles distribution for the three same total particle count. The histograms, represented in blue, orange and green, represent the probability for a nucleus to be crossed by a given number of particles. For each number of total particles, the corresponding Poisson distribution is drawn in red (dashed lines). µ is the mean number of particles crossing a voxel. Histogram 3c is obtained by simulating a layer of bdelloids and attaching a DoseToMedium scorer to every bdelloid voxel. PhaseSpace scorers are attached to three selected bdelloids to investigate the dose disparities at the nuclear level, leading to the histograms in Fig. 3d: a less irradiated bdelloid (in blue at 6.46 Gy), an average irradiated bdelloid (in green at 6.54 Gy) and a highly irradiated bdelloid (in red at 6.62 Gy). Fig. 3e uses a colormap to represent the dose distribution on an average irradiated bdelloid. Each color dot corresponds to a nucleus. The dose ranges from 1.95 to 11.97 Gy, with no nucleus receiving 0 Gy.

Simulation of desiccated bdelloids exposed to Fe radiation

A similar approach was applied to simulate the exposure of desiccated bdelloid to 0.5 GeV/n ^{56}Fe radiation. For the first part of the simulation, a single modeled bdelloid was exposed to an increasing number of ^{56}Fe particles. The DoseToMedium scorers attached to the nuclei retrieved the dose distribution over the bdelloid, as presented in Fig. 4a. At $2x10^3$ particles (the blue curve on Fig. 4a), 45% of nuclei scored 0 Gy. At $12x10^3$ (the orange curve on Fig. 4a), 0.64% of nuclei scored 0 Gy and at $23x10^3$ particles (the green curve on Fig. 4a), the dose ranges from 5.90 to 120.65 Gy, with a mean dose of 51.31 Gy. From these modeling results it was concluded that a 51.31 Gy dose is required to damage every nucleus in bdelloid individuals using 0.5 GeV/n ^{56}Fe particles.

Proton and ^{56}Fe particles both interact continuously with matter. Due to this property, the second readout of this simulation level yields identical results to the proton simulation. Particle distributions in this case are purely ballistic and do not depend on the nature of the ion. Similarly to the proton case, it is found that taking $\mu=23.7x10^3$ for the layer level ensures an average dose of 53.00 Gy and pushed 51.31Gy threshold-irradiated individuals at the lower end of the dose distribution.

In the third part of the simulation, a layer of desiccated bdelloids was modeled. As for the proton simulation, the results on Fig. 4c and 4d illustrate the diversity of irradiation among the layer of desiccated individuals. The simulation reaches the minimum 51.31 Gy threshold for all voxels. Histogram 4A represents the dose distribution over the bdelloids of a layer and ranges from 51.73 Gy to 56.20 Gy. No bdelloid scores 0 Gy. Histograms on Fig. 4c are obtained by assigning three PhaseSpace scorers to three different bdelloids: a less irradiated bdelloid (irradiated at 52.0 Gy, in blue), an average irradiated bdelloid (irradiated at 53.0 Gy, in green), and finally a highly irradiated bdelloid (irradiated at 54.0 Gy, in red). The PhaseSpace scorers serve as sources in bdelloid-level simulations to retrieve the dose distribution over the nuclei. The nuclei dose distributions are represented in blue (for less irradiated bdelloid in Fig. 4d), green (for average irradiated bdelloid in Fig. 4d) and red (highly irradiated bdelloid in Fig. 4d). No nucleus scored 0 Gy. The dose distribution over the nuclei is wider than the dose distribution over the bdelloids: 6.98 to 117.67 Gy for the nuclei of the less irradiated bdelloid, 6.02 Gy to 115.79 Gy for the average irradiated bdelloid and 6.34 Gy to 117.18 Gy for the highly irradiated bdelloid. Fig. 4e illustrates in a different way the dose repartition on the average irradiated bdelloid using a color map.

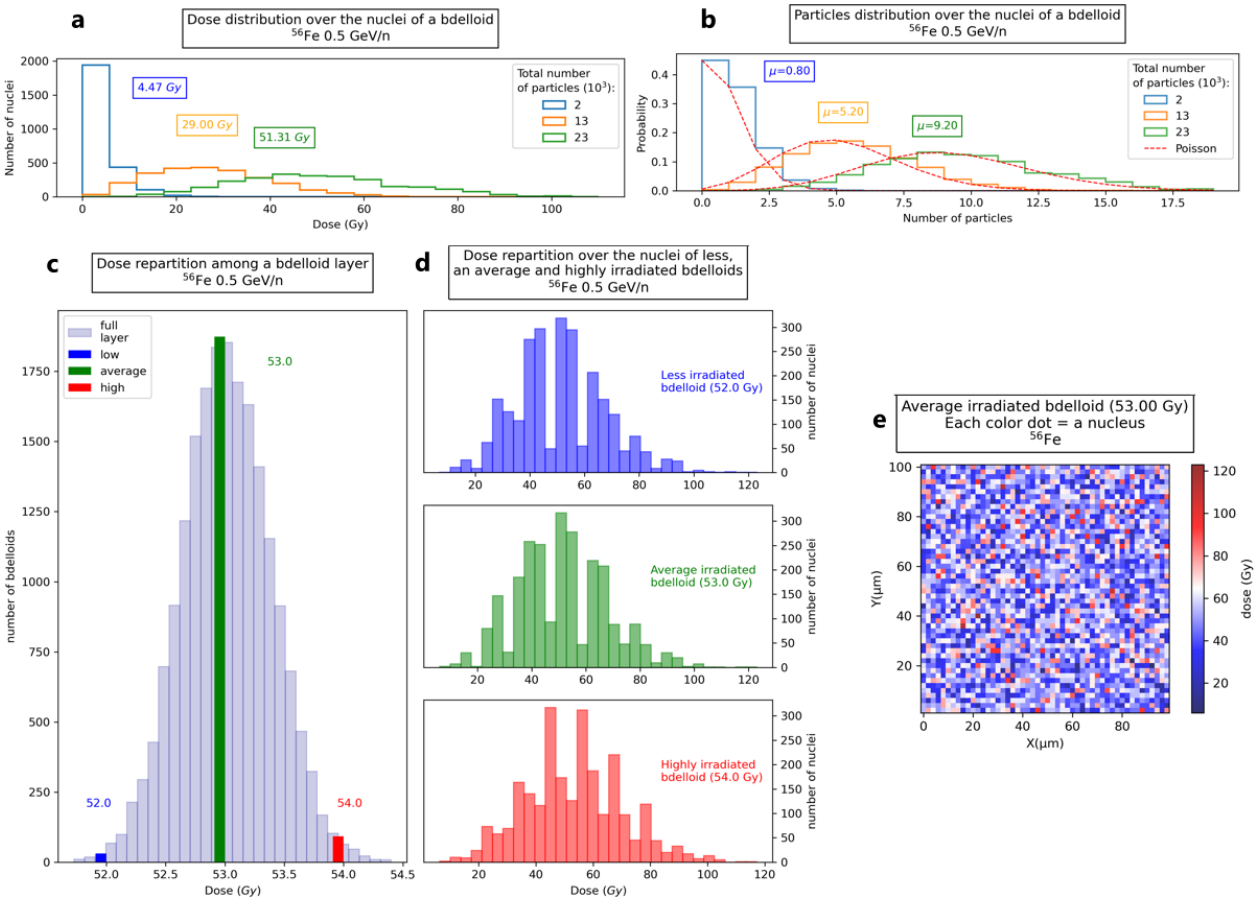

Fig. 4 Evaluating dose and particle distributions in modelled bdelloids at different irradiation levels of ^{56}Fe particles. Fig 4a presents the dose distribution for three different total particle counts. The histograms, represented in blue, orange and green, report the number of nuclei that have received a given dose. Fig. 4b presents the particles distribution for the three same total particle counts. The histograms, represented in blue, orange and green, represent the probability for a nucleus to be crossed by a given number of particles. For each number of total particles, the corresponding Poisson distribution is drawn in red (dashed lines). μ is the mean number of particles crossing a voxel. Histogram 4c is obtained by simulating a layer of bdelloids and attaching a DoseToMedium scorer to every bdelloid voxel. PhaseSpace scorers are attached to three selected bdelloids to investigate the dose disparities at the nuclear level, leading to the histograms in Fig. 4d: a less irradiated bdelloid (in blue at 52.0 Gy), an average irradiated bdelloid (in green at 53.0 Gy) and a highly irradiated bdelloid (in red at 54.0 Gy). Fig. 4e uses a colormap to represent the dose distribution on an average irradiated bdelloid. Each color dot corresponds to a nucleus. The doses range from 6.02 to 123.02 Gy, with no nucleus receiving 0 Gy.

Simulation of desiccated bdelloids exposed to 225 kVp X-rays

In contrast to proton and iron ions, X-ray particles do not interact continuously with matter. As a result, the presence or absence of damage in a nucleus is not solely determined by the crossing of a particle but also whether an interaction has occurred. Consequently, it is expected that more than 23×10^3 particles will be needed to damage all nuclei.

Fig. 5a illustrates the dose distribution across the nuclei at the rotifer level. At 0.01 Gy (corresponding to 1×10^8 particles), 0.36% of nuclei still score 0 Gy. 1.55×10^8 particles is the threshold above which all nuclei are damaged. The corresponding dose distribution ranges from 4.68×10^{-4} Gy to 8.67×10^{-2} Gy, with an average dose over the bdelloid of 0.02 Gy. This dose of 0.02 Gy is required to damage every nucleus in desiccated bdelloid individuals using 225 kVp

X-rays. Similarly, at 0.03 Gy (corresponding to $2x10^8$ particles), no nucleus scores 0 Gy, with a dose ranging from $1.62x10^{-3}$ to $1.74x10^{-1}$ Gy. Fig. 5b shows the particle distributions per voxel for an increasing number of incident particles. The three histograms correspond to $1.00x10^8$ (in blue), $1.55x10^8$ (in orange) and $2.00x10^8$ incident particles (in green). The corresponding Poisson distributions are drawn in red, with µ values of 40,000.27, 62,003.57 and 80,004.62 respectively.

To ensure a minimum dose of 0.02 Gy at the lower end of the layer dose distribution, all rotifers should be hit by a minimum of $6.2x10^4$ X-rays. Although conducting a full layer irradiation simulation would require 3 to 4 months of computation time, we can confidently estimate the dose received by the bdelloid layer based on the reliable results obtained from simulations with proton and ^{56}Fe particles. For instance, with an average layer dose of $2.67x10^{-2}$ Gy it is expected that all bdelloids are exposed to a non-zero dose of radiation and that 0.02 Gy threshold-irradiated individuals are pushed to the lower end of the dose distribution. Fig. 5c illustrates the dose repartition on the average irradiated ($2.67x10^{-2}$ Gy) bdelloid using a color map. The dose ranges from $24.79x10^{-5}$ to $11.53x10^{-2}$ Gy, but no nucleus scored 0 Gy.

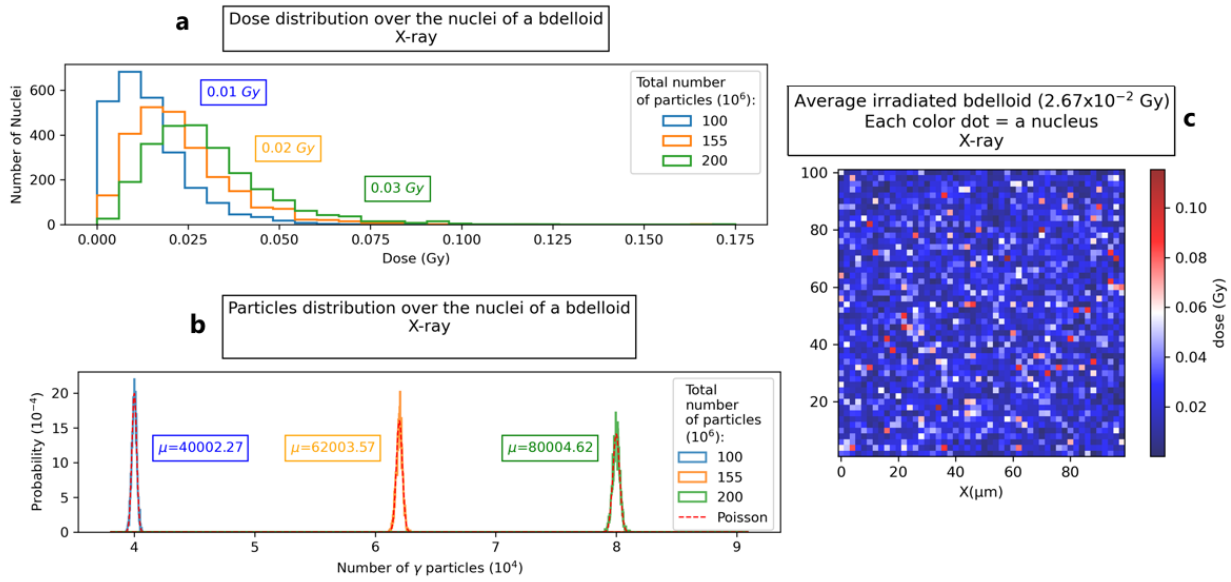

Fig. 5 Evaluation of dose and particles distribution of X-ray irradiated bdelloid level for three different total particle counts. The histograms, represented in blue, orange and green, count the number of nuclei that have received a given dose. Fig. 5b presents the particles distribution for the same three total particle counts. The histograms, represented in blue, orange and green, represent the probability for a nucleus to be crossed by a given number of particles. For each number of total particles, the corresponding Poisson distribution is drawn in red (dashed lines). µ is the mean number of particles crossing a voxel. Fig. 5c uses a colormap to represent the dose distribution on an average irradiated bdelloid. Each color dot corresponds to a nucleus. The dose ranges from $24.79x10^{-5}$ to $11.53x10^{-2}$ Gy, with no nucleus receiving 0 Gy.

Dose distribution at the nucleus level according to particle type

In addition to the above determined threshold doses ensuring irradiation of all nuclei of all rotifers in a layer, each one associated to a given particle type, the distribution patterns of energy deposition at the nucleus level are also valuable, as it can result in distinct biological responses. The third simulated level of granularity is thus a single nucleus of 2x2µm², segmented in 40x40

nm² voxels, representing the order of magnitude of the size of a DNA portion. Fig. 6 presents dose deposition maps for protons, ^{56}Fe and X-ray particles, at comparable doses of 55.10, 55.44 and 54.32 Gy respectively. The dose distributions exhibit striking differences: good homogeneity for X-rays, sparsity for protons with unaffected DNA regions, and highly localized energy deposits for ^{56}Fe ions. In the case of charged particles, the primary particles are responsible for most of the damage, while secondary particles, such as electrons, contribute negligibly to the dose accumulation (as visualized by the light-yellow spots corresponding to secondary electrons for ^{56}Fe irradiation in Fig. 6).

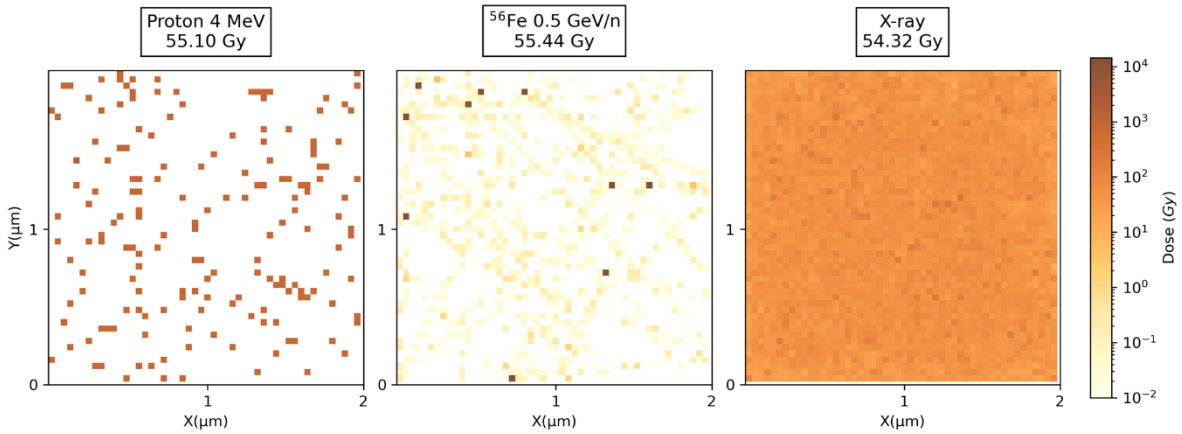

Fig. 6 Views of the dose distribution for proton, ^{56}Fe and X-ray radiation at nucleus level. Comparable doses of 55.10, 55.44 and 54.32 Gy respectively are attained. The squares represent bdelloid nuclei of 2x2 µm², segmented in 40x40 nm² voxels. Voxels share a common color scale, representing the amount of dose deposited within it, ranging from 0 Gy (white), to 1,45x10⁴ Gy (dark brown).

Discussion

In 2020, Hespeels et al., characterized the biological response of desiccated *A. vaga* individuals to high doses of low and high LET radiation including X-rays, 4 MeV protons and 0.5 GeV/n Fe particles. Experiments showed that desiccated *A. vaga* individuals have a lethal dose range of 5,000 to 7,500 Gy when exposed to low and high LET radiation. Specifically, the survival rate at a dose of 5,000 Gy was significantly higher for animals exposed to X-ray radiation (82.7% SD ± 11.4) than to proton radiation (19.1% SD ± 34.1) (Hespeels et al. 2020). This finding was consistent with the concept of relative biological effectiveness, which suggests that high LET radiation is more biologically damaging than low LET radiation (Goodhead 1999). Secondly, results showed a clear difference between low and high LET radiation at the reproductive level. A 2.3 factor was reported when comparing SD50 (sterilization dose 50, i.e., the dose of radiation required to sterilize 50% of the population) of X-rays versus protons and Fe particles.

The progressive decline in fertility of irradiated bdelloids has been previously attributed to the accumulation of cellular damage, particularly DNA damage. When exposed to radiation beyond a certain threshold, the ability of bdelloids to efficiently repair their damaged cells is compromised, leading to sterility. Alternatively, two hypotheses have been proposed to explain the decline with increasing dose observed in previous studies. The first hypothesis suggests that some bdelloids could be partially or completely spared by radiation due to statistical disparities across the bdelloid layer. Secondly, germinal cells of certain bdelloids may remain unaffected

by the radiation, preventing sterilization. However, as the radiation dose increases, every nucleus of every bdelloid would gradually be impacted, ultimately leading to total sterilization. Simulations in Topas are powerful tools to understand this difference and, more generally, to provide an insight into the sterilization mechanism.

To evaluate the validity of the two alternative hypotheses, all three radiation qualities (protons, iron ions, and X-rays) and the exposure of desiccated bdelloid were modeled. The DoseToMedium scorer was used on the entire layer of bdelloids to calculate the global dose, and voxel subdivision was used to determine the dose distribution over individual bdelloids. The PhaseSpace scorer was then used on a bdelloid from the layer as a source to simulate the individual level, which enabled subdivision of the bdelloid into nuclei voxels to determine the dose distribution over all the nuclei. This method enables the verification of whether germinal cell nuclei are spared or not. By iteratively adjusting the number of particles and evaluating the nuclear damage (reported as energy deposition events, leading ultimately to damage on biological molecules, such as DNA) on selected bdelloid individuals, the threshold dose above which all nuclei cells (in both somatic and germinal cells) are exposed can be determined. If these dose thresholds are significantly lower than the SD50 and the doses used in experiments, it would rule out both hypotheses. Thus, simulations were used to determine the minimum macroscopic dose (threshold dose) required on a bdelloid layer to ensure that every nucleus of all bdelloids receives a minimum dose greater than 0 Gy. The same method was used for every particle. Data were summarized in table 1.

	Particles threshold (bdelloid level)	*Dose threshold (bdelloid level) (Gy)*	*Particles threshold (layer level)*	*Dose threshold (layer level) (Gy)*
Protons 4 MeV	$2.3x10^{4}$	2.99	$2.37x10^{4}$	3.00
^{56}Fe 0.5 GeV/n	$2.3x10^{4}$	51.31	$2.37x10^{4}$	53.00
X-Rays 225 kVp	$1.52x10^{8}$	$2.00x10^{-2}$	$1.521x10^{8}$	$2.67x10^{-2}$

Table 1 Summary of Topas simulation data. Comparison of particles and dose thresholds associated with Proton, Fe and X-rays radiation.

Here, Topas simulations highlight that exposure to P+ 4MeV, 0.5 GeV/n ^{56}Fe, and X-ray radiation at doses of 3.00 Gy, 53.00 Gy, and $2.67x10^{-2}$ Gy, respectively, effectively hit all individuals, cells, and nuclei within the samples. All these values were far under the level of dose required to observe any biological response in our previous results supporting the idea that impact of the radiation on the survival rate or fertility rate was indeed associated with the damage induced by the radiation and not by absence of hit in some individuals or germinal cell nuclei. For example, no impact on reproductive level was reported until 250 Gy for Proton and Fe exposure and until 750 Gy for X-ray (Hespeels et al. 2020). Doses of at least 1 mGy have been previously shown to induce DNA double-strand breaks (DSBs). Furthermore, a linear relationship between DSB induction and dose has been reported in the past (Rothkamm et Löbrich 2003). Therefore, we definitively excluded that some bdelloids were not hit or some germinal cells were not affected by radiation experiments previously published.

Particle radiation generates a unique form of DNA damage through the creation of numerous ionizations localized along the path of the particle through the cell. These damages are not evenly distributed and vary greatly depending on the linear energy transfer (LET) of the

radiation. Low-LET radiation results in diffuse damage, while high-LET radiation generates clusters of different types of damage, such as base lesions, abasic sites, single-strand breaks (SSBs), and double-strand breaks (DSBs), which are collectively referred to as complex DNA damage. Understanding the nature of radiation is essential in predicting the type and extent of DNA damage. Here Topas software was used to visualize the distribution of dose deposition within a single bdelloid nucleus. Our results confirm that high-LET particles, such as Fe and protons, generate more localized dose deposition along the particle track than low-LET X-ray radiation (Fig. 6). Indeed, the pattern generated by Topas simulations is consistent with the biological response observed in desiccated bdelloids exposed to low and high-LET radiation. Previous attempts to experimentally visualize different types of DNA damage induced by proton and X-ray radiation on desiccated bdelloids support the variation in genomic integrity between samples irradiated by both sources of radiation (Hespeels et al. 2020). The increased amount of short-sized DNA fragments reported after proton exposure, compared to X-ray irradiated samples, was previously attributed to the clustered damages generated by proton exposure, resulting in a higher relative biological effectiveness of proton radiation versus X-rays. However, quantifying short DNA fragments induced by radiation remains a challenging task (Höglund et al. 2000; Alloni et al. 2013; Barbieri et al. 2019). The complexity of damage caused by high-LET radiation is a crucial factor for understanding the effects of radiation exposure, as it can reduce survival rates and the capacity to produce viable offspring in desiccated bdelloids. Our simulation results confirm previous observations and emphasize the importance of understanding the nature of radiation in predicting the type and extent of DNA damage.

In the absence of techniques that enable the examination of specific damage from each type of radiation, employing simulation approaches offers valuable understanding of the physical processes at play in the methods applied to desiccated bdelloid specimens. This approach can also be expanded to include other metazoans like tardigrades, which have been previously utilized as a reference for radiotolerance. Incorporating a model into simulations inherently creates some divergence between our experiment design, as simulated by Topas, and actual samples. However, it is crucial to emphasize that replicating every real-world constraint is impossible. For example, our model constrains the nucleus size to a 2 µm square, which may not precisely represent real-world conditions, given that genomic material compaction degree and volume extent can differ between cell types and developmental stages. Estimation based on *A. vaga* microscopy captures revealed that germinal cell nuclei were approx. 2 µm diameter as our model. However, most of the somatic cell nuclei range approx. 3 µm and germovitellarium cell nuclei were closed to 4 µm (Terwagne et al. 2022). Therefore, despite these limitations, we have confidence in the model's ability to closely approximate the average structural features previously documented in desiccated bdelloids. Finally, it is essential to emphasize that our TOPAS model focused on the description of energy deposition in simulated rotifers, without providing specific data on the resulting damage from dose deposition. Ionizing radiation damage to biological samples can occur through two distinct pathways. Based on *direct damage*, we inferred a connection between dose deposition and DNA damage, but additional factors might significantly impact the biological response. The second pathway, called *indirect action*, involves generating effectors such as reactive oxygen species (ROS), which are often produced through water radiolysis due to incident radiation, subsequently damaging cellular components (Dartnell 2011). The proportion of water molecules was found to be 94% in hydrated *A. vaga* individuals and approximately 6.5% in desiccated samples,

indicating significant targets for interaction with ionizing radiation. While it was not feasible to simulate and quantify here the contribution of these elements to the biological response of irradiated bdelloids, the localization of indirect damage is anticipated to follow the pattern of *Low LET, sparse localization* vs. *High LET, clustered damage*. In conclusion, investigating the complexity of damage induced at the cellular level, encompassing proteins and membranes, remains a critical aspect of future research, alongside DNA damage characterization.

By showcasing the differential impact of low and high LET radiation on desiccated bdelloid rotifer samples, the current study opens new avenues for exploration in subsequent research. Key questions to explore include the specific repair mechanisms triggered by different types of radiation-induced damage, as well as how these mechanisms are regulated. Furthermore, it remains unknown how radiation resistance pathways and specific molecular actors themself are impacted by increasing doses of radiation and may be ultimately inactivated. Additionally, it is important to discriminate between DNA repair mechanisms occurring in somatic cells versus germ cells, as this distinction may have significant implications for the understanding of survival and reproduction data. How are the various types of damage repaired? Can we observe any differences in the genomes of the offspring of irradiated organisms? Several ongoing studies employing transcriptomic and comparative genomic approaches should provide more insights into these matters. Among ongoing experiments, these questions are being tackled in the unique environment of space during experiments taking place on board the International Space Station (ISS) and will evaluate the impact of microgravity on the DNA repair system of *A. vaga* species. Furthermore, examining the repair of such damage across different bdelloid species, both resistant and sensitive to desiccation and irradiation, may help refine our understanding of the mechanisms that enable these animals to withstand massive doses of ionizing radiation. This unique ability sets bdelloid rotifers apart in the animal kingdom.

Conclusion

In this study, the impact of radiation exposure on bdelloid rotifers was simulated, examining whether every nucleus is equally affected or if some rotifers are partially or entirely spared based on parameters used in previously published studies (Hespeels et al. 2014; 2020). Additionally, the research aimed to correlate biological data with energy deposition patterns induced by low and high linear energy transfer (LET) radiation, using simulations of protons, iron ions, and X-rays. Our simulations demonstrated that exposure to 4 MeV protons, 0.5 GeV/n 56-Fe, and X-ray radiation from doses of 3.00 Gy, 53.00 Gy, and 2.67×10^{-2} Gy, respectively, uniformly affected all individuals, cells, and nuclei within the samples. Data indicate that radiation's impact on survival and fertility rates in bdelloid rotifers stems from radiation-induced damage, ruling out the possibility of unaffected rotifers or germinal cells in previous studies, as all administered doses were above the biological response threshold. Furthermore, our simulations unveiled substantial differences between low and high LET radiation in terms of irradiated individuals' nuclei. Simulations verified the sparse versus diffuse distribution of radiation hits among cell nuclei when exposed to high or low LET radiation, respectively. In summary, our simulations support the notion that the diminished fertility observed in high LET-exposed samples is associated with complex DNA damage due to the concentrated energy deposition pattern of high-LET radiation compared to low LET.

Acknowledgements

The authors thank the European Space Agency (ESA) and the Belgian Federal Science Policy Office (BELSPO) for their support in the framework of the PRODEX Program.

Statements and Declarations

The authors declare that they have no competing interests.

References

Agostinelli, S., J. Allison, K. Amako, J. Apostolakis, H. Araujo, P. Arce, M. Asai, et al. 2003. « Geant4—a Simulation Toolkit ». *Nuclear Instruments and Methods in Physics Research Section A: Accelerators, Spectrometers, Detectors and Associated Equipment* 506 (3): 250-303. https://doi.org/10.1016/S0168-9002(03)01368-8.

Allison, J., K. Amako, J. Apostolakis, H. Araujo, P. Arce Dubois, M. Asai, G. Barrand, et al. 2006. « Geant4 Developments and Applications ». *IEEE Transactions on Nuclear Science* 53 (1): 270-78. https://doi.org/10.1109/TNS.2006.869826.

Allison, J., K. Amako, J. Apostolakis, P. Arce, M. Asai, T. Aso, E. Bagli, et al. 2016. « Recent Developments in Geant4 ». *Nuclear Instruments and Methods in Physics Research Section A: Accelerators, Spectrometers, Detectors and Associated Equipment* 835 (novembet): 186-225. https://doi.org/10.1016/j.nima.2016.06.125.

Alloni, D., A. Campa, W. Friedland, L. Mariotti, et A. Ottolenghi. 2013. « Integration of Monte Carlo Simulations with PFGE Experimental Data Yields Constant RBE of 2.3 for DNA Double-Strand Break Induction by Nitrogen Ions between 125 and 225 KeV/Mm LET ». *Radiation Research* 179 (6): 690-97. https://doi.org/10.1667/R3043.1.

Alpert, Peter. 2005. « The Limits and Frontiers of Desiccation-Tolerant Life ». *Integrative and Comparative Biology* 45 (5): 685-95. https://doi.org/10.1093/icb/45.5.685.

Barbieri, Sofia, Gabriele Babini, Jacopo Morini, Werner Friedland, Manuela Buonanno, Veljko Grilj, David J. Brenner, Andrea Ottolenghi, et Giorgio Baiocco. 2019. « Predicting DNA Damage Foci and Their Experimental Readout with 2D Microscopy: A Unified Approach Applied to Photon and Neutron Exposures ». *Scientific Reports* 9 (1): 14019. https://doi.org/10.1038/s41598-019-50408-5.

Beltrán-Pardo, Eliana, K. Ingemar Jönsson, Mats Harms-Ringdahl, Siamak Haghdoost, et Andrzej Wojcik. 2015. « Tolerance to Gamma Radiation in the Tardigrade *Hypsibius Dujardini* from Embryo to Adult Correlate Inversely with Cellular Proliferation ». *PloS One* 10 (7): e0133658. https://doi.org/10.1371/journal.pone.0133658.

Crowe, John H. 2014. « Anhydrobiosis: An Unsolved Problem ». *Plant, Cell & Environment* 37 (7): 1491-93. https://doi.org/10.1111/pce.12304.

Dartnell, Lewis R. 2011. « Ionizing Radiation and Life ». *Astrobiology* 11 (6): 551-82. https://doi.org/10.1089/ast.2010.0528.

« Desiccation tolerance of prokaryotes: application of principles to human cells - PubMed ». Consulted the 18th may 2023. https://pubmed.ncbi.nlm.nih.gov/21676831/.

« Extreme Resistance of Bdelloid Rotifers to Ionizing Radiation ». Consulted the 18th of may 2023. https://doi.org/10.1073/pnas.0800966105.

Faddegon, Bruce, José Ramos-Méndez, Jan Schuemann, Aimee McNamara, Jungwook Shin, Joseph Perl, et Harald Paganetti. 2020. « The TOPAS Tool for Particle Simulation, a Monte Carlo Simulation Tool for Physics, Biology and Clinical Research ». *Physica Medica: PM: An International Journal Devoted to the Applications of Physics to Medicine and Biology: Official Journal of the Italian Association of Biomedical Physics (AIFB)* 72 (april): 114-21. https://doi.org/10.1016/j.ejmp.2020.03.019.

Fischer, Claus, Wilko H. Ahlrichs, Anita G. J. Buma, Willem H. van de Poll, et Olaf R. P. Bininda-Emonds. 2013. « How Does the "ancient" Asexual *Philodina Roseola* (*Rotifera: Bdelloidea*) Handle Potential UVB-Induced Mutations? » *The Journal of Experimental Biology* 216 (Pt 16): 3090-95. https://doi.org/10.1242/jeb.087064.

« Gateway to genetic exchange? DNA double-strand breaks in the bdelloid rotifer *Adineta vaga* submitted to desiccation - Hespeels - 2014 - Journal of Evolutionary Biology - Wiley Online Library ». Consulted the 18th of may 2023. https://onlinelibrary.wiley.com/doi/full/10.1111/jeb.12326.

Gladyshev, Eugene A., et Irina R. Arkhipova. 2010. « Genome Structure of Bdelloid Rotifers: Shaped by Asexuality or Desiccation? » *Journal of Heredity* 101 (suppl_1): S85-93. https://doi.org/10.1093/jhered/esq008.

Goodhead, D. T. 1999. « Mechanisms for the Biological Effectiveness of High-LET Radiations ». *Journal of Radiation Research* 40 Suppl (december): 1-13. https://doi.org/10.1269/jrr.40.s1.

Gusev, Oleg, Yuichi Nakahara, Veronica Vanyagina, Ludmila Malutina, Richard Cornette, Tetsuya Sakashita, Nobuyuki Hamada, Takahiro Kikawada, Yasuhiko Kobayashi, et Takashi Okuda. 2010. « Anhydrobiosis-Associated Nuclear DNA Damage and Repair in the Sleeping Chironomid: Linkage with Radioresistance ». *PLOS ONE* 5 (11): e14008. https://doi.org/10.1371/journal.pone.0014008.

Hagiwara, Yoshihiko, Takahiro Oike, Atsuko Niimi, Motohiro Yamauchi, Hiro Sato, Siripan Limsirichaikul, Kathryn D. Held, Takashi Nakano, et Atsushi Shibata. 2019. « Clustered DNA Double-Strand Break Formation and the Repair Pathway Following Heavy-Ion Irradiation ». *Journal of Radiation Research* 60 (1): 69-79. https://doi.org/10.1093/jrr/rry096.

Hespeels, Boris, Sébastien Penninckx, Valérie Cornet, Lucie Bruneau, Cécile Bopp, Véronique Baumlé, Baptiste Redivo, et al. 2020. « Iron Ladies – How Desiccated Asexual Rotifer *Adineta vaga* Deal With X-Rays and Heavy Ions? » *Frontiers in Microbiology* 11. https://www.frontiersin.org/articles/10.3389/fmicb.2020.01792.

Höglund, E., E. Blomquist, J. Carlsson, et B. Stenerlöw. 2000. « DNA Damage Induced by Radiation of Different Linear Energy Transfer: Initial Fragmentation ». *International Journal of Radiation Biology* 76 (4): 539-47. https://doi.org/10.1080/095530000138556.

Joiner, Michael C., et Albert J. van der Kogel. 2018. *Basic Clinical Radiobiology*. CRC Press.

Jönsson, K. Ingemar, et Andrzej Wojcik. 2017. « Tolerance to X-Rays and Heavy Ions (Fe, He) in the Tardigrade *Richtersius Coronifer* and the Bdelloid Rotifer *Mniobia Russeola* ». *Astrobiology* 17 (2): 163-67. https://doi.org/10.1089/ast.2015.1462.

Judson, Olivia P., et Benjamin B. Normark. 1996. « Ancient Asexual Scandals ». *Trends in Ecology & Evolution* 11 (2): 41-46. https://doi.org/10.1016/0169-5347(96)81040-8.

Lehnert, Shirley. 2007. *Biomolecular Action of Ionizing Radiation*. CRC Press.

Leprince, Olivier, et Julia Buitink. 2015. « Introduction to Desiccation Biology: From Old Borders to New Frontiers ». *Planta* 242 (2): 369-78. https://doi.org/10.1007/s00425-015-2357-6.

Lomax, M. E., L. K. Folkes, et P. O'Neill. 2013. « Biological Consequences of Radiation-Induced DNA Damage: Relevance to Radiotherapy ». *Clinical Oncology* 25 (10): 578-85. https://doi.org/10.1016/j.clon.2013.06.007.

Mattimore, V, et J R Battista. 1996. « Radioresistance of *Deinococcus radiodurans*: functions necessary to survive ionizing radiation are also necessary to survive prolonged desiccation ». *Journal of Bacteriology* 178 (3): 633-37. https://doi.org/10.1128/jb.178.3.633-637.1996.

Mavragani, Ifigeneia V., Zacharenia Nikitaki, Spyridon A. Kalospyros, et Alexandros G. Georgakilas. 2019. « Ionizing Radiation and Complex DNA Damage: From Prediction to Detection Challenges and Biological Significance ». *Cancers* 11 (11): 1789. https://doi.org/10.3390/cancers11111789.

Maynard Smith, John. 1986. « Evolution: Contemplating Life without Sex ». *Nature* 324 (6095): 300-301. https://doi.org/10.1038/324300a0.

Melone, Giulio, et Diego Fontaneto. 2005. « Trophi Structure in Bdelloid Rotifers ». *Hydrobiologia* 546 (september): 197-202. https://doi.org/10.1007/s10750-005-4197-z.

Pagani, Manuela, Claudia Ricci, et Carlo Redi. 1993. « Oogenesis in *Macrotrachela quadricornifera* (*Rotifera, Bdelloidea*) - I. Germarium eutely, karyotype and DNA content ». *Hydrobiologia* 255-256 (april): 225-30. https://doi.org/10.1007/BF00025843.

Perl, J., J. Shin, J. Schumann, B. Faddegon, et H. Paganetti. 2012. « TOPAS: An Innovative Proton Monte Carlo Platform for Research and Clinical Applications ». *Medical Physics* 39 (11): 6818-37. https://doi.org/10.1118/1.4758060.

Poludniowski, G., G. Landry, F. DeBlois, P. M. Evans, et F. Verhaegen. 2009. « SpekCalc: A Program to Calculate Photon Spectra from Tungsten Anode x-Ray Tubes ». *Physics in Medicine & Biology* 54 (19): N433. https://doi.org/10.1088/0031-9155/54/19/N01.

Poludniowski, Gavin G. 2007. « Calculation of X-Ray Spectra Emerging from an x-Ray Tube. Part II. X-Ray Production and Filtration in x-Ray Targets ». *Medical Physics* 34 (6): 2175-86. https://doi.org/10.1118/1.2734726.

Poludniowski, Gavin G., et Philip M. Evans. 2007. « Calculation of X-Ray Spectra Emerging from an x-Ray Tube. Part I. Electron Penetration Characteristics in x-Ray Targets ». *Medical Physics* 34 (6): 2164-74. https://doi.org/10.1118/1.2734725.

Potts, M. 1994. « Desiccation Tolerance of Prokaryotes ». *Microbiological Reviews* 58 (4): 755-805. https://doi.org/10.1128/mr.58.4.755-805.1994.

Potts, Malcolm, Stephen M. Slaughter, Frank-U. Hunneke, James F. Garst, et Richard F. Helm. 2005. « Desiccation Tolerance of Prokaryotes: Application of Principles to Human Cells ». *Integrative and Comparative Biology* 45 (5): 800-809. https://doi.org/10.1093/icb/45.5.800.

Ramos-Méndez, J., N. Domínguez-Kondo, J. Schuemann, A. McNamara, E. Moreno-Barbosa, et Bruce Faddegon. 2020. « LET-Dependent Intertrack Yields in Proton Irradiation at Ultra-High Dose Rates Relevant for FLASH Therapy ». *Radiation Research* 194 (4): 351-62. https://doi.org/10.1667/RADE-20-00084.1.

Rebecchi, Lorena, Roberto Guidetti, Simona Borsari, Tiziana Altiero, et Roberto Bertolani. 2006. « Dynamics of Long-Term Anhydrobiotic Survival of Lichen-Dwelling Tardigrades ». *Hydrobiologia* 558 (1): 23-30. https://doi.org/10.1007/s10750-005-1415-7.

Ricci, Claudia. 2017. « Bdelloid rotifers: 'sleeping beauties' and 'evolutionary scandals', but not only ». *Hydrobiologia* 796 (july). https://doi.org/10.1007/s10750-016-2919-z.

Ricci, Claudia, Manuela Caprioli, Chiara Boschetti, et Nadia Santo. 2005. « *Macrotrachela quadricornifera* featured in a space experiment ». *Hydrobiologia* 534 (february): 239-44. https://doi.org/10.1007/s10750-004-1509-7.

Ricci, Claudia N. 1987. « Ecology of Bdelloids: How to Be Successful ». *Hydrobiologia* 147 (1): 117-27. https://doi.org/10.1007/BF00025734.

Ricci, Claudia, et Manuela Pagani. 1997. « Desiccation of *Panagrolaimus rigidus* (*Nematoda*): Survival, reproduction and the influence on the internal clock ». *Hydrobiologia* 347 (january): 1-13. https://doi.org/10.1023/A:1002979522816.

Rothkamm, Kai, et Markus Löbrich. 2003. « Evidence for a Lack of DNA Double-Strand Break Repair in Human Cells Exposed to Very Low x-Ray Doses ». *Proceedings of the National Academy of Sciences of the United States of America* 100 (9): 5057-62. https://doi.org/10.1073/pnas.0830918100.

Segers, Hendrik. 2007. « Annotated checklist of the rotifers (*Phylum Rotifera*), with notes on nomenclature, taxonomy and distribution ». *Zootaxa* 1564 (august): 1-104. https://doi.org/10.11646/zootaxa.1564.1.1.

Semenenko, V. A., et R. D. Stewart. 2004. « A Fast Monte Carlo Algorithm to Simulate the Spectrum of DNA Damages Formed by Ionizing Radiation ». *Radiation Research* 161 (4): 451-57. https://doi.org/10.1667/rr3140.

Terwagne, Matthieu, Emilien Nicolas, Boris Hespeels, Ludovic Herter, Julie Virgo, Catherine Demazy, Anne-Catherine Heuskin, Bernard Hallet, et Karine Van Doninck. 2022. « DNA Repair during Nonreductional Meiosis in the Asexual Rotifer *Adineta Vaga* ». *Science Advances* 8 (48): eadc8829. https://doi.org/10.1126/sciadv.adc8829.

Ward, J. F. 1994. « The Complexity of DNA Damage: Relevance to Biological Consequences ». *International Journal of Radiation Biology* 66 (5): 427-32. https://doi.org/10.1080/09553009414551401.

Section 3: Space simulation

The previous article provided a study of the effects of radiation exposure on bdelloid rotifers, investigating the relationship between biological data and patterns of energy deposition. These particles, specifically protons and ^{56}Fe, hold particular importance in the context of space, as they can contribute significantly to the overall dose output. Therefore, their contribution will be differentiated in the results of this last section that focuses on space environment simulations.

Introduction

The Oltaris online tool was utilized to simulate the space radiation environment that will be experienced by the bdelloid samples in the International Space Station. Oltaris offers various environment selections and geometry options. In addition to the Earth orbit of the International Space Station (ISS), environments on the Moon and Mars can be simulated, as well as solar particle events (SPE). Two approaches are employed for the analysis. In both approaches, a reproduction of the sample carrier geometry that will be used in Rotifer-A is uploaded to Oltaris. In the first approach, Oltaris provides direct dose outputs in the rotifer samples. In the second approach, environments from Oltaris are retrieved at the samples' boundaries, and the dose output is calculated using Topas simulations. The Oltaris approach provides estimations for longer exposure periods, such as dose per year, allowing assessment of radiation levels over extended durations. On the other hand, Topas enables a more detailed analysis, providing differentiated contributions at the cost of a smaller exposure time.

First, a description of the module geometry is provided, followed by an overview of the Oltaris tool, its usage, and the resulting outputs. Then, the implementation procedure of Oltaris outputs in Topas using the environment sources is explained. Additionally, technical considerations are presented to address the challenges of simulating long exposure times in Topas with a fully modeled module. The process of ray tracing the geometry is then detailed, showcasing how a complex geometry can be uploaded and utilized in Oltaris. Dose outputs from Oltaris and Topas are then compared, showcasing the differences between shieled and unshielded rotifer patches in the module. Finally, the results are discussed, and a fertility and survival time limits are estimated.

Materials and Methods

The Space module description and its modeling in Topas

Achieving meaningful results hinges on creating an accurate model of the space module that houses the bdelloids. However, it's important to note that this module's design is still in its initial phases, and it could change in the future. The model is based on the most recent and reliable design, furnished by the engineering firm in charge of constructing the module. Therefore, the current model should be viewed as a provisional representation and not the final design. The modeled module is represented in Fig. 5. The design philosophy for the ROTIFER experiment container is as follows: a common module (CM) will be fixed on the NanoRack external platform of the ISS. The CM is designed to contain two smaller scientific modules (SM1 and SM2), each with their own design and geometry to hold several experiments. The ROTIFER experiment will be situated in the SM2 module.

The CM, SM2 and the ROTIFER experimental setup have been accurately modeled in Topas. The CM is approximated as an empty aluminum box measuring 762.0 x 998.0 x 488.4 mm^3,

with 30 mm thick walls. Additional components, such as electronics or fixation modules have been omitted from the model. As the exact placement of the SM2 within the CM is unspecified, it is assumed to be in the center, aligned with the surface of the CM. The SM2 module is modeled as a 150x150x150 mm^3 aluminum cube, with 12 mm thick walls. The thermal sensor, pressure gauge and valve have not been modeled. A sealed 105x105x38 mm^3 volume within the upper half of the SM2 contains two levels of 36 wells measuring 12 mm in diameter and 10 mm in depth. The bottom wells correspond to *dark* samples that will be isolated from solar light, while the upper wells are *light* samples that will be exposed to external light but are protected from vacuum by a MgF_2 windows. A 105x105x36 mm^3 aluminum plate marks the separation between the bottom and upper wells, and an additional drilled aluminum plate is modeled on top of the light wells. The MgF_2 windows are assumed to be the same thickness as the drilled aluminum plate, and fit into its holes, covering the sun wells. The placement of the wells inside of the sealed volume has been established according to the reference model datasheet (see Fig. 5). Inside of the wells, desiccated bdelloid samples are modeled using our standard 30 µm thick and human skin material. Their radius is set to 6 mm to fit into the well.

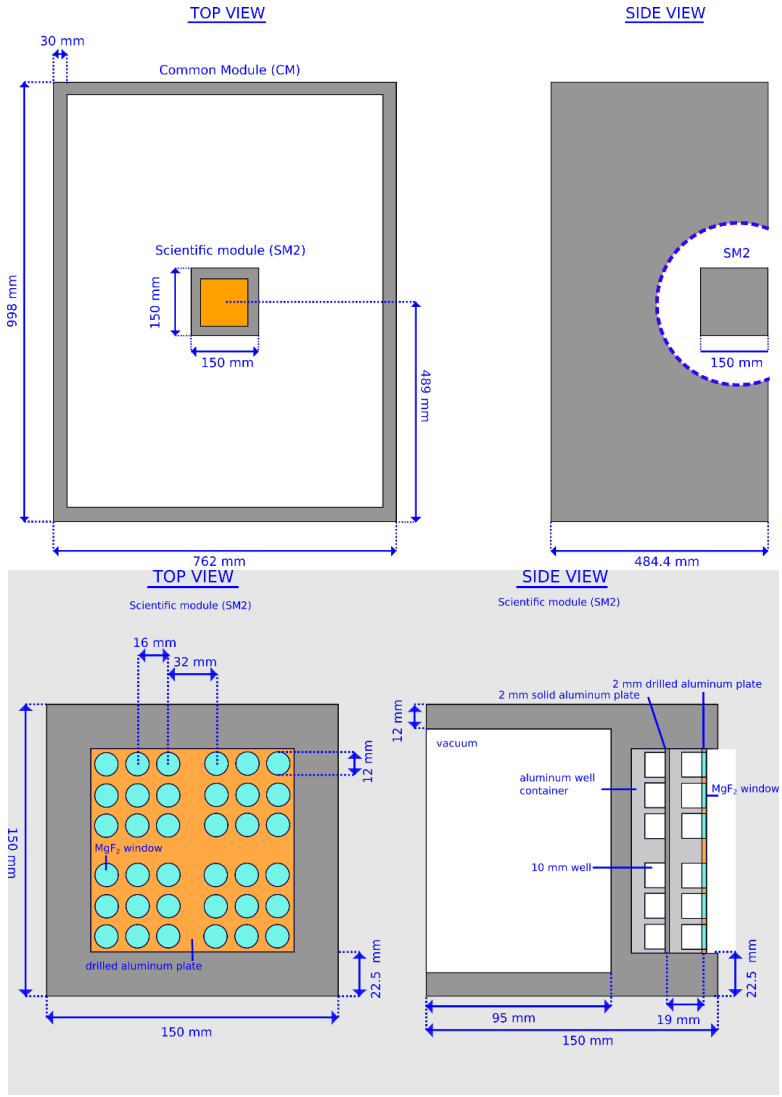

Fig. 5 Top and side views of the modeled common module (CM) and Scientific module (SM2). Due to a lack of information concerning the insertion of the SM2 inside of the CM, the SM2 is centered and adjacent to the top surface of the CM . The reference model datasheets are in the appendix. Note that the SM2 dark and light grey structures are aluminum, the color difference being only useful for modeling clarity purposes.

Oltaris and the simulated space environment

Oltaris (Online Tool for the Assessment of Radiation in Space) is an online tool developed by *NASA* that utilizes the Fortran radiation transport algorithms *HZETRN2005* and *NUCFRG2* to estimate the effects of space radiative environment on humans and objects during space travels (Singleterry et al. 2010). Oltaris provides an accessible approach by offering modular, user-selected (1) radiation environments, (2) materials, (3) transport geometries, and (4) response functions. These parameters are selected on the Oltaris website (« OLTARIS Home Page » 2023), and the calculation is executed on a computational cluster.

(1) There are different types of radiation environments available: Solar Particle Events (SPE), free-space Galactic Cosmic Rays (GCR), trapped protons within the earth's magnetic field, albedo neutrons from the Earth's atmosphere, Lunar Surface, and Earth Orbit (EO). The latter is a combination of SPE, GCR, trapped protons and albedo neutrons with selectable mission dates, altitude, and inclination. The environment output is given as spectral flux or fluences in $particles \cdot cm^{-2} \cdot AMeV^{-1} \cdot time^{-1}$, *AMeV* being the energy (in *MeV*) by nucleon of a particle. SPE occurs when many charged particles (mainly protons) in the sun's atmosphere are accelerated by its magnetic field. SPE are rare events, that occur statistically seven times a year, but can significantly increase the radiation intensity (Jiggens et al. 2014). Trapped protons refer to the protons trapped in the Earth's geomagnetic field. Albedo neutrons result from the interaction of GCR with the Earth's atmosphere. Several GCR Badhwar-O'Neil models are available that include the contribution of solar winds (T. C. Slaba et Whitman, 2020). These models fit balloon and satellite measured energy spectra from 1954 to 1992, but also measurements from the Advanced Composition Explorer satellite from 1997 to 2002, within a <10% margin of average relative error (Singleterry et al. 2010; T. Slaba et Whitman 2020). The Badhwar-O'Neil model is regularly updated as new data becomes available.

(2) Materials are defined by selecting elemental mass percentages, molecular mass percentages or chemical formulas. Once defined, a material is submitted to the cluster that generates a cross sections database (Singleterry et al. 2010). The material cross sections are used by Oltaris to predict the way in which neutrons and charged particles will interact with the material. More specifically, it is the probability of interaction between a particle projectile and the target nucleus with a particular outcome. An example of computed cross section for the aluminum material would be:

$$^{56}\mathrm{Fe} + ^{27}\mathrm{Al} \rightarrow {}^{12}\mathrm{C} + {}^{\mathrm{A}}_{\mathrm{Z}}X$$

Where X are leftover projectile and target fragments.

(3) Transport geometry refers to the geometry of simulated objects travelling through space. Interaction of particles in the geometry element is computed by the transport algorithm. There are two types of geometries: the first one is thickness distributions which are suited for complex geometries and whose cross-sections are computed using a ray tracing process. The ray tracing process utilizes rays to travel through the geometry and retrieve the materials and thicknesses encountered. The second one is material slabs. Material slabs are simple, layered objects, such as a sphere with multiple shells.

(4) Response functions provide an output similar to Topas's scorers. They are attached to the transport geometry. Among the several response functions available, only the Differential Flux/Fluence and Dose response function were used. The fluence response function outputs the flux of particles (in $particles \cdot AMeV^{-1} \cdot day^{-1} \cdot cm^{-2}$ for most environments, and in $particles * AMeV^{-1} * event^{-1} * cm^{2}$ for SPE) at each material interface in the transport geometry.

Earth orbit model

To replicate the trajectory of the bdelloids outside the International Space Station, a Circular Earth Orbit model (CEO) is selected. The associated GCR model is Badhwar-O'NEil 2020, valid through December 2018 (T. Slaba et Whitman 2020). Consequently, the trajectory was set to begin on 12/01/2018 and to end on 12/31/2018. The altitude was set at 400 km to match the ISS altitude, with an inclination of 51.6°. The Aerospace corporation Proton version 8 (AP8) trapped model was also selected to retrieve trapped proton and neutron albedo effects. The Differential Flux/Fluence response function was used to register the differential flux and fluence of particles at the boundary of the module or bdelloid samples in a DAT format. The DAT files are processed in python to be used as PhaseSpace sources in Topas. An exhaustive description of the computational procedure under Oltaris's Earth orbit model can be found in (Badavi et al. 2006; King 2012; J. Wilson et denn 1976; J. W. Wilson et al. 2006; J. W. Wilson, Townsend, et Farhat 1989; Foelsche et al. 1974; Townsend et al. 2003)

The radiative environment provided by Oltaris is represented in Fig. 6a and the corresponding energy spectra on Fig. 6b

A

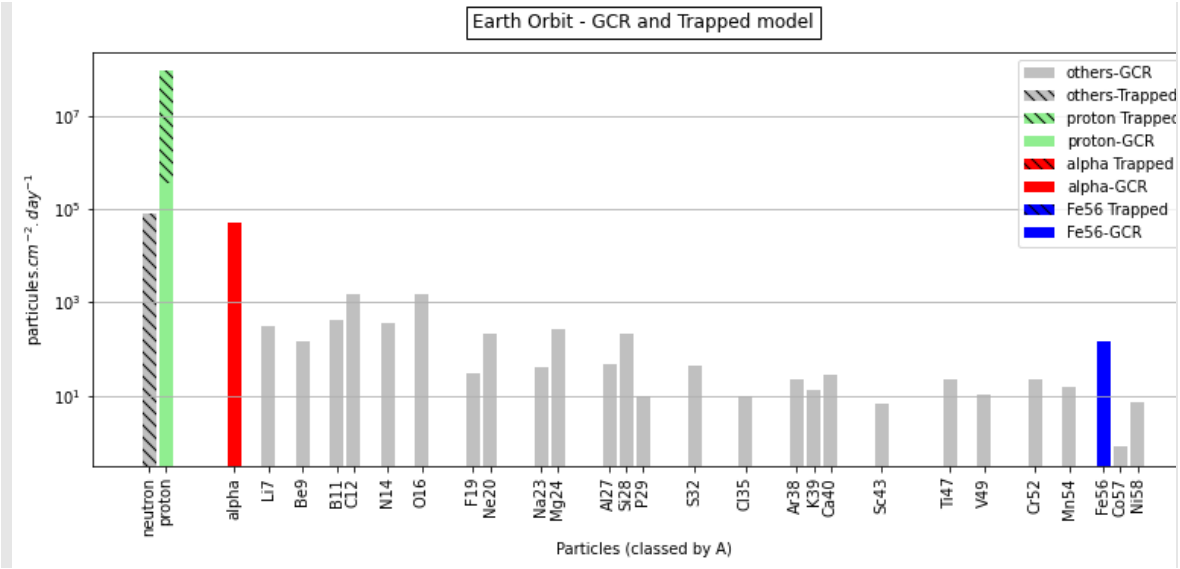

B

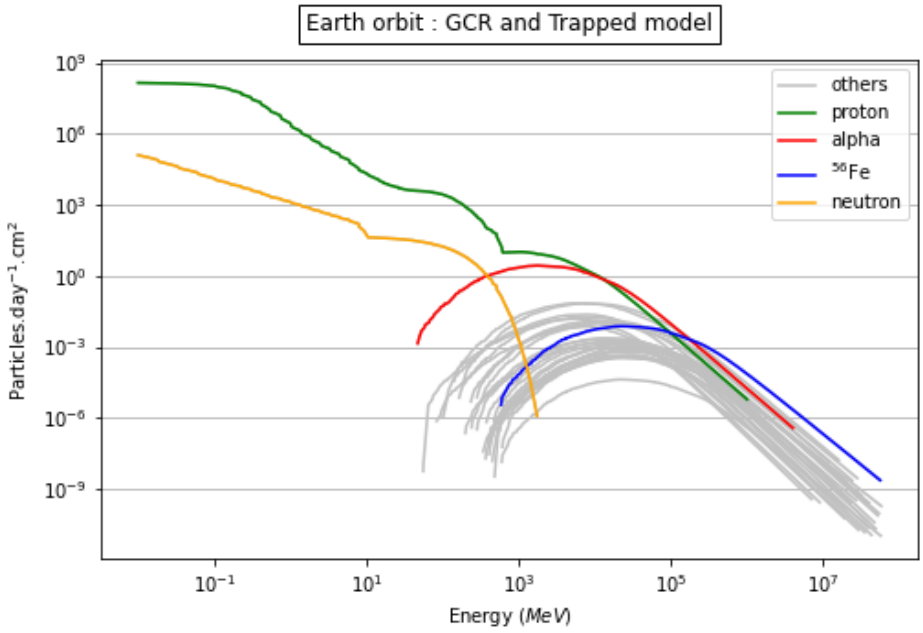

Fig. 6 Radiative environments provided by Oltaris. Fig 6a shows the particle composition of the GCR environment. The proton has a higher proportion than other particles (one order of magnitude more). Among the high Z particles, the proportion of ^{56}Fe is of importance. Fig 6b shows the same GCR composition but with the associated energy spectra.

Lunar Surface

When using a raytraced geometry, the free space GCR environment is applied to geometry components mapped with upward facing rays. Albedo, the byproduct of GCR interaction with

lunar regolith is applied to geometry elements mapped with downward facing rays. It is mainly composed of secondary particles emitted upwards (with unknown level of uncertainty). The orientation of the geometry element with respect to the lunar surface is defined with a vector in Oltaris. As for Earth, lunar GCR environment is based on Badhwar O'Neil model and has been applied for a one-month mission duration (December 2018). and is accurate within 10% or less. The basic structure and mathematics used to describe the lunar surface environment as input to OLTARIS has been described by Clowdsley et al. (2005). Fig. 7a shows the particle distribution of the Moon surface environment whereas Fig 7b presents the energy spectra of the particles.

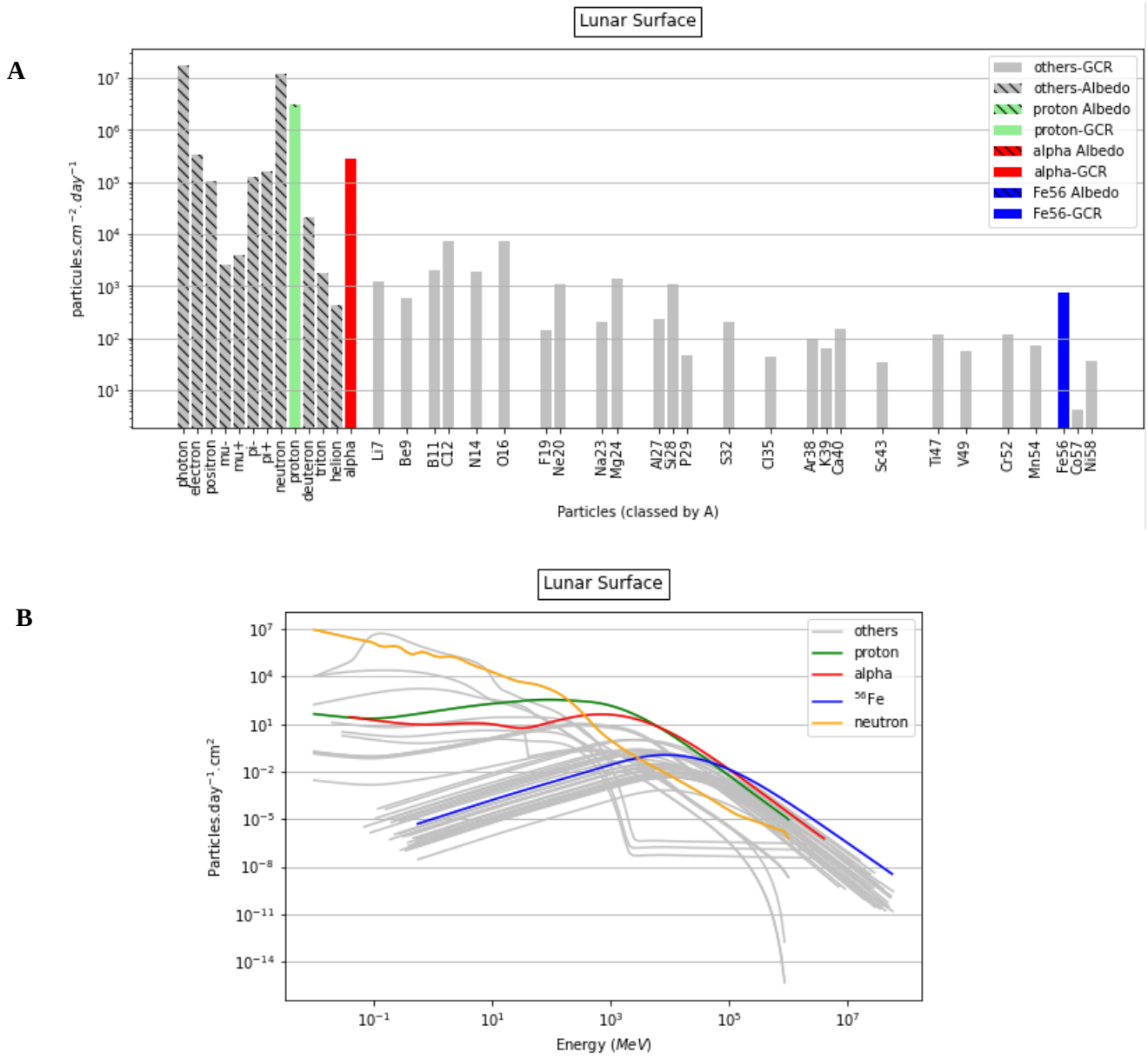

Fig. 7 Lunar GCR and Albedo compositions. The GCR is similar in its relative composition to the Earth GCR but has more particles overall. The lunar albedo consists of light elements: photons, electrons, positrons, etc. Although more numerous than the GCR, the albedo particles are mostly low LET radiation. Figure 7b exhibit the lunar surface composition but with associated energy spectra.

GCR on Mars surface

A Mars surface simulation in Oltaris consists of two phases. First, the particles fluences are retrieved by combining atmosphere and albedo particles at 1 meter above the Martian surface. The composition of the Martian atmosphere is based on Angelis et al. (2004) and is comprised of 95% CO_2, 2.70 % N_2, 1.6% Ar, 0.13% O2 and 0.08% CO for a density of $1.86 * 10^{-6} g/cm^3$. The thickness of the atmosphere as a function of surface elevation is computed using the Mars-GRAM 2001 model, which is an average of the thickness.

The resulting point fluence serves as the basis of the environment for the module geometry. Fig 8a shows the composition of the Mars surface environment. The whole spectrum of particles from photon to Ni58 is present and, similar to the Moon surface, a large variety of light particles can be found, including photons, neutrons, electrons, etc. Fig 8b presents the energy spectra of the particles.

A

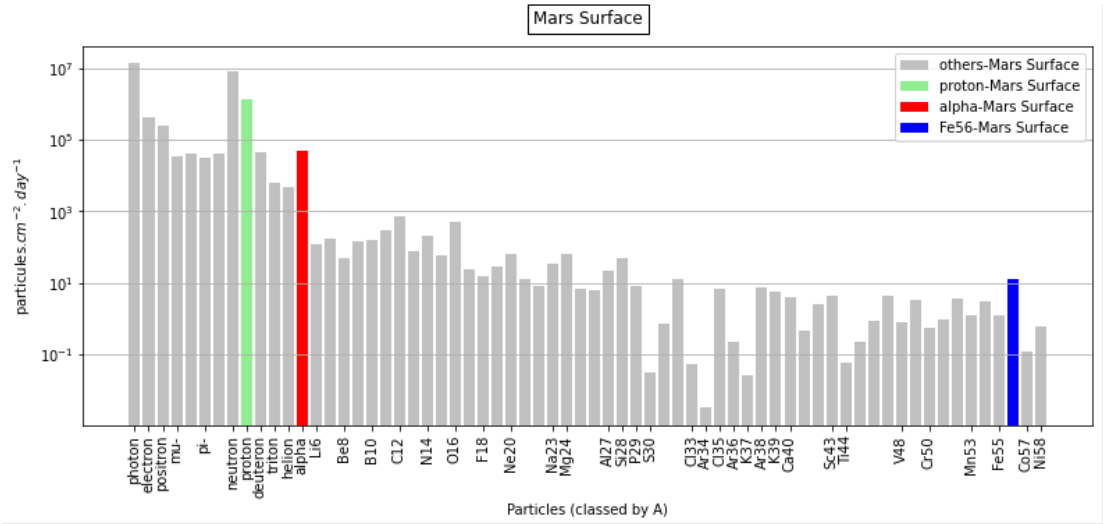

B

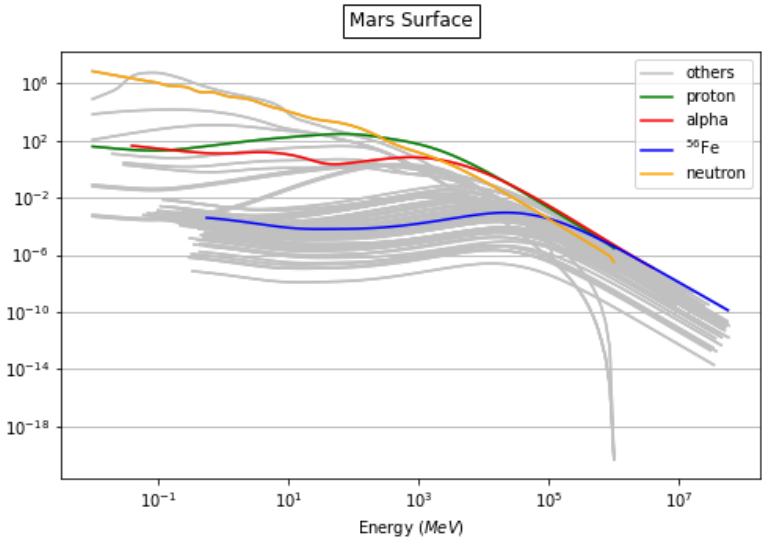

Fig. 8 Figure 8a presents the particle spectrum of the Mars surface environment. The spectrum covers the totality of the isotopes from the proton to the Ni58. The Mars environment is also rich in light particles such as photons and electrons. As Oltaris provides a single environment without differentiation of GCR and Albedo component is not possible. Figure 7b exhibit the lunar surface composition but with associated energy spectra.

Earth, SPE

Solar Particle Events are available for free space environments at 1 AU ($1.5 * 10^8$ km). All SPE environments are based on detailed analytical fits to ground based or space borne measurements. There are two options: user defined SPE, where the user can use Oltaris curve fit tools to define a SPE, or Historical SPE, an option where the user can choose any combination of events to include in the SPE environment, and multiply or attune them. The historical October 1989, introduced in section 1, has been chosen with a 1 factor. The basic structure and mathematics used to describe the SPE environment as input to Oltaris has also been described in (Badavi et al. 2006). SPE environments output fluxes in $particles * AMeV^{-1} * cm^{-2} * event^{-1}$. SPE output provided by Oltaris for Earth, Moon and Mars environment are identical. Indeed, all are referred to as free space SPE. The only difference with Martian and lunar environments being the inclusion of their albedo in the environment. Fig 9 shows the energy distribution of an SPE event. The fluences are in $Particles * event^{-1} * cm^{-2}$

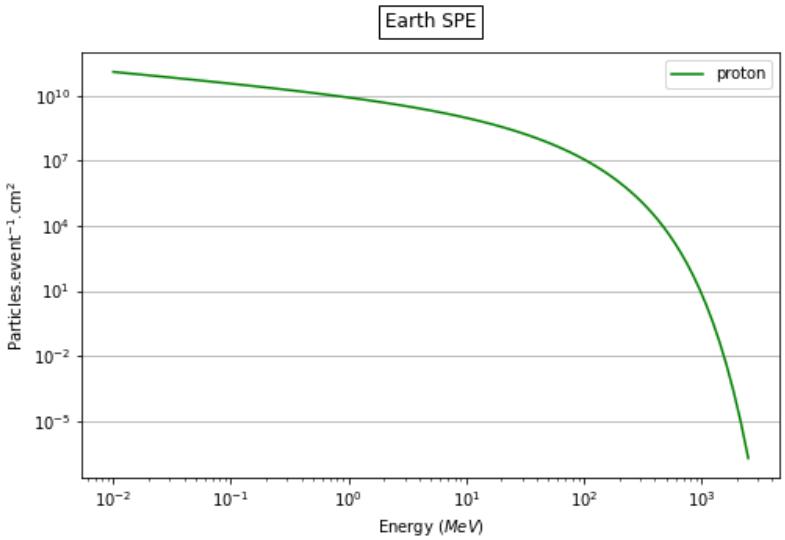

Fig. 9 SPE energy spectrum, with protons fluences in particles per event per cm^2. There are many protons below 4 MeV, the studied energy for proton in section 2. Low energy protons have smaller penetration capabilities and are likely to be stopped by the aluminum shielding of the dark patches.

Irradiation of space module into Topas

Environment sources in Topas are specifically designed for scenarios involving spacecraft transport radiation and other similar situations (« Environment Source — TOPAS 3.8 documentation » 2022). They create an isotropic (same fluences from all directions), uniform (same fluences outputs at any point in the geometry) radiation field enclosing a specified component designed by the user. Topas automatically generates the smallest sphere that encompasses the component, and particles are emitted from the surface of the sphere towards its interior, following a cosine angular distribution (Lambert's cosine law). This approach guarantees the creation of a homogeneous environment, essential for accurate simulations. Each

particle has an energy array in *MeV*, a weight array representing the normalized spectrum, and a total number of particles to be simulated in a run.

Oltaris provides a common *AMeV* (energy in *MeV* per nucleon) energy spectrum for all particles involved in the spatial environment. Fluence for a given particle at a specific energy of the spectrum is provided in $particles * AMeV^{-1} * day^{-1} * cm^{-2}$. An Oltaris particle can be implemented in Topas using the following approach: Firstly, the *MeV* array is generated by multiplying the common *AMeV* energy range by the particle's mass number. Then, the weights can be obtained by normalizing the fluence spectrum. To determine the total number of particles to simulate, the fluence spectrum needs to be multiplied by the mission duration, the particle's mass number and the surface area of the environment sphere. To manage computational resources efficiently, it is crucial to minimize the radius of the environment sphere as much as possible. Indeed, the total number of particles to simulate is proportional to the square of the sphere radius.

There are various possible options to consider when determining the Topas simulation geometry. Our initial approach involved modeling the entire module, both SM2 and CM, in Topas and simulating an environment source around. The corresponding radius of the environment source was 0.67 m. This approach offers valuable insights on the particle behavior throughout the entire module. For instance, it enables the investigation of particle stopping within the module's shielding and the identification of interactions leading to the generation of secondary particles. However, using a 0.67 m radius would result in an unreasonable number of particles, even for short exposures. Considering a fully parallelized simulation with 24 CPU threads, the particle simulation rate is approximately $8 * 10^6$ particles per hour. Table 2 shows the estimated simulation times (ST) for a second of irradiation time (IT):

	Particles per day/event	*ST for 1s of IT (hour)*
Earth orbit	$5.0x10^{12}$	7
Lunar surface	$1.4x10^{12}$	2
Mars surface	$3.6x10^{11}$	1/2
SPE	$2.6x10^{16}$	*35 942*

Table 2 Estimation of simulation times for various Oltaris environments. Although some are reasonably achievable, the simulation times become unreasonable to simulate one day, let alone one month.

Additionally, the Mars, Moon and Earth spectra contain very few instances of specific particles. Consequently, the total number of simulated particles cannot fall below a certain threshold that would compromise the integrity and proportionality of the spectrum. The minimal simulation time required for Earth is approximately 14 hours, while for the Moon it is around 40 minutes, and 244 hours for Mars. Based on these considerations, it becomes clear that although simulating the entire module allows for an in-depth study of particle interactions, this method is not suitable for simulating long-duration scenarios. Extrapolating Topas results, such as dose deposition and interaction data, from short periods of less than a second to a few months or years, can be highly unreliable without further insight.

Ray tracing of space module in Oltaris

An alternative approach involves leveraging the computational power of Oltaris to handle the module geometry, complementing the Topas simulation. In this method, Oltaris allows the user to specify thickness distribution elements with points of interest corresponding to the rotifer samples. This method enables to retrieve the irradiation spectrum directly at the boundary of the rotifers. Assuming a homogeneous fluence within the rotifer volume, these spectra can be implemented as environments in Topas. In that case, there is no need to implement the entire module geometry in Topas; only the rotifer sample needs to be included. This leads to a significantly smaller environment sphere with a radius of 8.49 mm. By reducing the radius from 0.67 m to 8.49 mm, which is approximately a ~79-fold reduction, the squared factor results in a total reduction of approximately 6,241 for the simulation time.

Moreover, Oltaris offers the capability to provide dose estimations in units of dose per day, month, or year. These dose calculations are based on human tissue materials, but it is reasonable to assume that they are comparable to the human skin material utilized for the rotifers in our study. These dose estimations can serve as valuable reference points for extrapolating and validating the outputs obtained from Topas simulations.

Implementing geometry in Oltaris can be challenging, especially for complex geometries. While simple geometries like slabs or spheres are available natively on the Oltaris website, with a limited range of materials, implementing thickness distributions for more intricate geometries requires the use of raytraced geometries. This concept is exemplified in Fig .10a, where a target point, or bdelloid patch in our case, serves as the source of a ray distribution. As the rays traverse the patch, they intersect geometry elements, capturing the thickness and material between consecutive intersections. Complex geometries can be accurately mapped by employing a significant number of rays. The retrieved thickness distributions for each bdelloid patch are then compiled into a single XML file, which can be uploaded to Oltaris for subsequent simulations. While Oltaris does not offer a built-in raytrace algorithm or software, it provides ray distributions in the form of *dat* files. Those *dat* files contain the cosine values of the $[x, y, z]$ components of the ray direction, which will be referred to as the $[a, b, c]$ direction. Two types of ray distributions available: latitude-longitude and geodesic ray distributions. Since latitude-longitude distributions are denser at the equator and sparser at the poles, which is not desirable for the module geometry, we opted for a geodesic distribution. Geodesic distributions provide a more uniform angular coverage. In this case, we specifically choose the geodesic distribution with 1002 rays due to computational considerations.

A

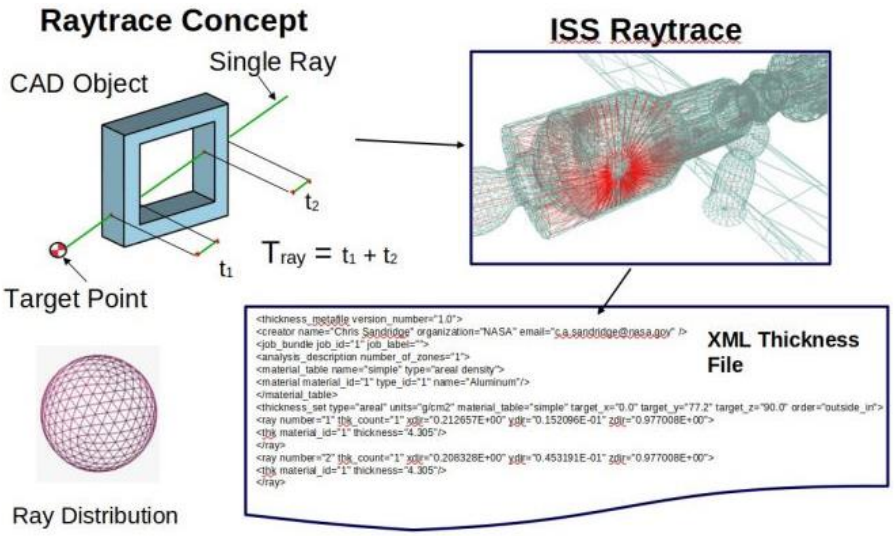

B

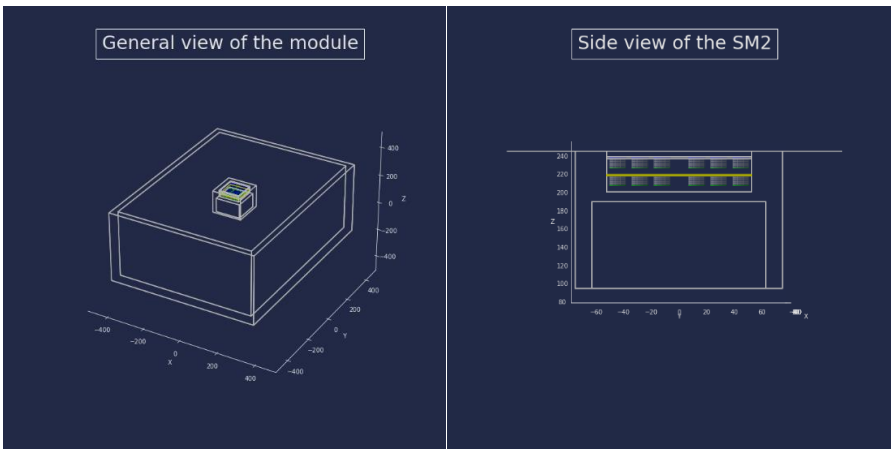

Fig. 10 Fig 10a shows the thickness distribution geometry philosophy on Oltaris. First, a target point is defined in a geometry and a ray stores the thicknesses and materials along its path. The process is repeated for each ray in a ray distribution and the result is stored in a XML thickness file. Fig 10b shows the reconstruction of the module in python, using cubes and cylinder classes.

Next, Python was utilized to model and perform raytracing on the module geometry. The modeling process involved defining a cube class with half-lengths $[HLX, HLY, HLZ]$, a center position $[x_c, y_c, z_c]$ and a corresponding material. Similarly, a cylinder class was established, incorporating a radius, a *HLZ* half-length, $[x_c, y_c, z_c]$ center position, and a material. Fig. 10b showcases the outcome of the modeling process, presenting the resulting geometry representation. Next, a ray class is implemented, which possesses a ray origin $[x_0, y_0, z_0]$ and a ray direction $[a, b, c]$ derived from Oltaris rays' distribution. Once the ray is initialized, the goal is to mathematically find the intersections between the ray and the module's geometry. The mathematical treatment differs depending on whether the intersection occurs with a cube or a cylinder. It is important to note that all geometry elements are aligned along the z-axis, which eliminates the need for coordinate system transformations during each collision detection. To begin, we can express the parametric equation of the ray, which describes the ray's path through space:

$$\begin{bmatrix} x \\ y \\ z \end{bmatrix} = \begin{bmatrix} x_0 \\ y_0 \\ z_0 \end{bmatrix} + t * \begin{bmatrix} a \\ b \\ c \end{bmatrix}$$

With *t* the distance traveled along the normalized ray direction [*a*, *b*, *c*]. Let us consider a cubic geometry element and suppose that we wish to detect the intersections of the ray with its *x*-oriented surfaces. The x-oriented surfaces are parts of two infinite *x*-oriented planes of equations $x_- = x_c - HLX$ and $x_+ = x_c + HLX$. The algorithm 1 outlined below effectively detects these intersections:

Algorithm 1: Intersection of the ray with a cubic geometry element

```
1   Input: [a, b, c] and [x_0, y_0, z_0] vectors and x_-, x_+, y_-, y_+, z_-, z_+ limits
2   Output: all intersection points [x, y, z]
3   for Cube geometries:
4       t ← (x_- − x_0)/a
5       if t > 0:
6           y ← y_0 + b * t
7           z ← z_0 + c * t
8           if y_- ≤ y ≤ y_+ and z_- ≤ z ≤ z_+:
9               [x, y, z] is an intersection
10          end
11      end
12  end
```

In practice, rounding errors can occur, necessitating the inclusion of a tolerance parameter at line ***8*** (1e-9 mm was used). A similar algorithm can be applied to detect intersections with *y* and *z*-oriented planes. Detecting intersections with cylinders is relatively straightforward when we differentiate the problem into the (x, y) plane and the *z*-oriented surfaces. Since the cylinders are all aligned along the *z*-axis, they appear as circles in the (x, y) plane. The equation of a circle, $(x - x_c)^2 + (y - y_c)^2 = r^2$, can then be used to identify the intersections with the cylinder with algorithm 2:

Algorithm 2: Intersection of the ray with a cylindric geometry element

```
1   Input: [a, b, c] and [x_0, y_0, z_0] vectors and r, z_-, z_+ limits
2   Output: all intersection points [x, y, z]
3   for Cylinder geometries:
4       t_1, t_2 ← solve (x_0 + a * t − x_c)^2 + (y_0 + b * t − y_c)^2 = r * 2
5       if t_1 ≥ 0 :
6           z ← z_0 + b * t_1
7           if z_- ≤ z ≤ z_+:
8               [x, y, z] is an intersection
9           end
10      end
11      if t_2 ≥ 0 :
12          repeat 6 to 9 with t_2
13  end
```

The detection of intersections with *z*-oriented surfaces of cylinders follows the same algorithm as that used for cube. However, in Algorithm 1, line ***8*** is modified as follows: ***if*** $(x_0 + a * t)^2 + (y_0 + b * t)^2 \leq r^2$. To determine the thickness of the material between two consecutive intersection distances, $t_1$and t_2, the average distance $t = \frac{t_1+t_2}{2}$ is computed. This average distance is used to calculate the associated $[x, y, z]$ coordinates and identify the corresponding geometry element along with its associated material. The set of thicknesses *t* and their associated materials are then transposed in XML format, adhering to the guidelines specified by Oltaris. The MgF_2 and rotifer materials are separately defined using online native tools of Oltaris. Following the upload of the XML file, the thickness distribution becomes available for all Oltaris projects.

Results

Earth orbit

Fig. 11 presents the results of the Oltaris and Topas simulations. The squared map, on the right of the figures, represents the SM2 module whereas the color dots represent the bdelloid patches. The color scale is common for every simulated environment and represents the received dose in mGy. Although Oltaris outputs daily, monthly, and yearly dose estimations, the monthly dose output was presented as it corresponds to the limits of validity of the Badhwar-O'Neil model. The light patches (upper figure) are only isolated from the space environment by MgF2 windows, whereas the dark patches (lower figure) are more in depth in the SM2 and protected from the sunlight by a layer of Aluminum. For each light and dark patches, a simulation is run in Topas from the particle fluences provided by Oltaris to differentiate the contribution of the different particles to the total dose. The Topas simulation are computed for one day of space exposition and are systematically measured for the same selected rotifer sample, chosen for its average position. The monthly dose on the light rotifer computed by Oltaris is 13.614 ± 0.127 mGy, (± 0.127 being the standard deviation) for the light patches and 9.739 ± 0.167 mGy for the dark patches. The dose contribution comes mainly from the trapped model (≈78% of the total dose in both cases). Topas simulation, on the other hand, outputs a daily dose of 8.52 mGy for the light samples and 6.44 mGy for the darks, which, extrapolated, gives a monthly dose of 255.6 mGy and 193.2 mGy respectively. Topas simulation also provides some insight on the contribution of different particles to the total dose. The contribution is made at ~90% of protons (88.4%), iron (1.8%) and alphas (2.1%) in the light case and 85% protons, 2.3% iron and 2.7% alphas in the dark case.

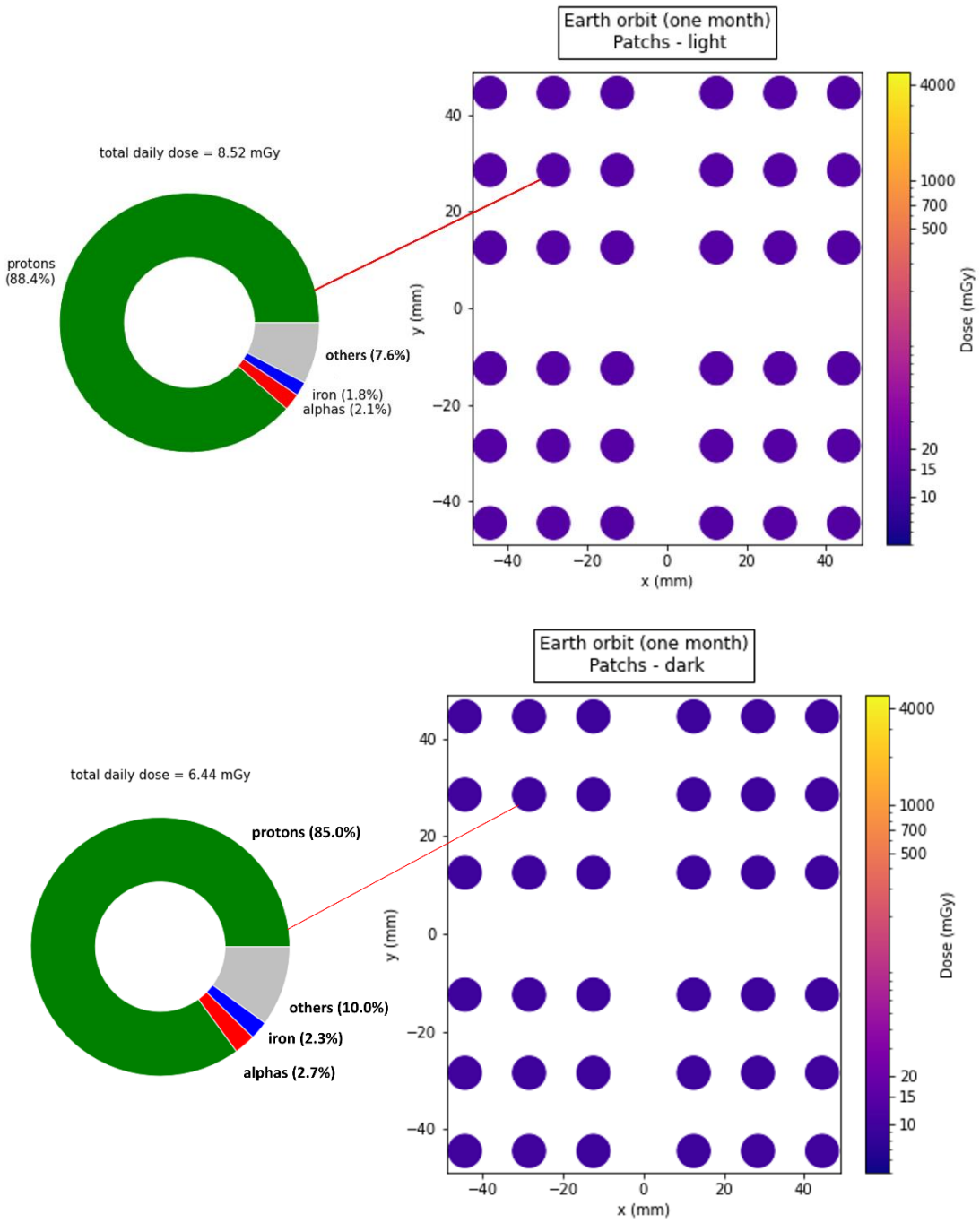

Fig. 11 Results of Oltaris and Topas for an Earth orbit environment. The right colormaps, obtained with Oltaris, show the irradiation of the rotifer samples, whereas the pie charts on the left, obtained with Topas, differentiate the contribution of the different particles. For this environment, protons are the main source of radiation. The colorbar scale is common for all environments. Others refers to the ions from the GCR spectrum and neutrons from the trapped model that can be seen on Fig. 6.

Additionally, and exclusively for the Earth orbit simulation due to time limitations, the Topas daily dose has been computed for every rotifer patch, both light and dark. The resulting repartition of dose is represented on Fig. 12. The rotifers samples are sorted from least irradiated to most irradiated. Fig. 12 confirms that the relative contributions of the particles are in similar proportion for all patches, both lights and darks.

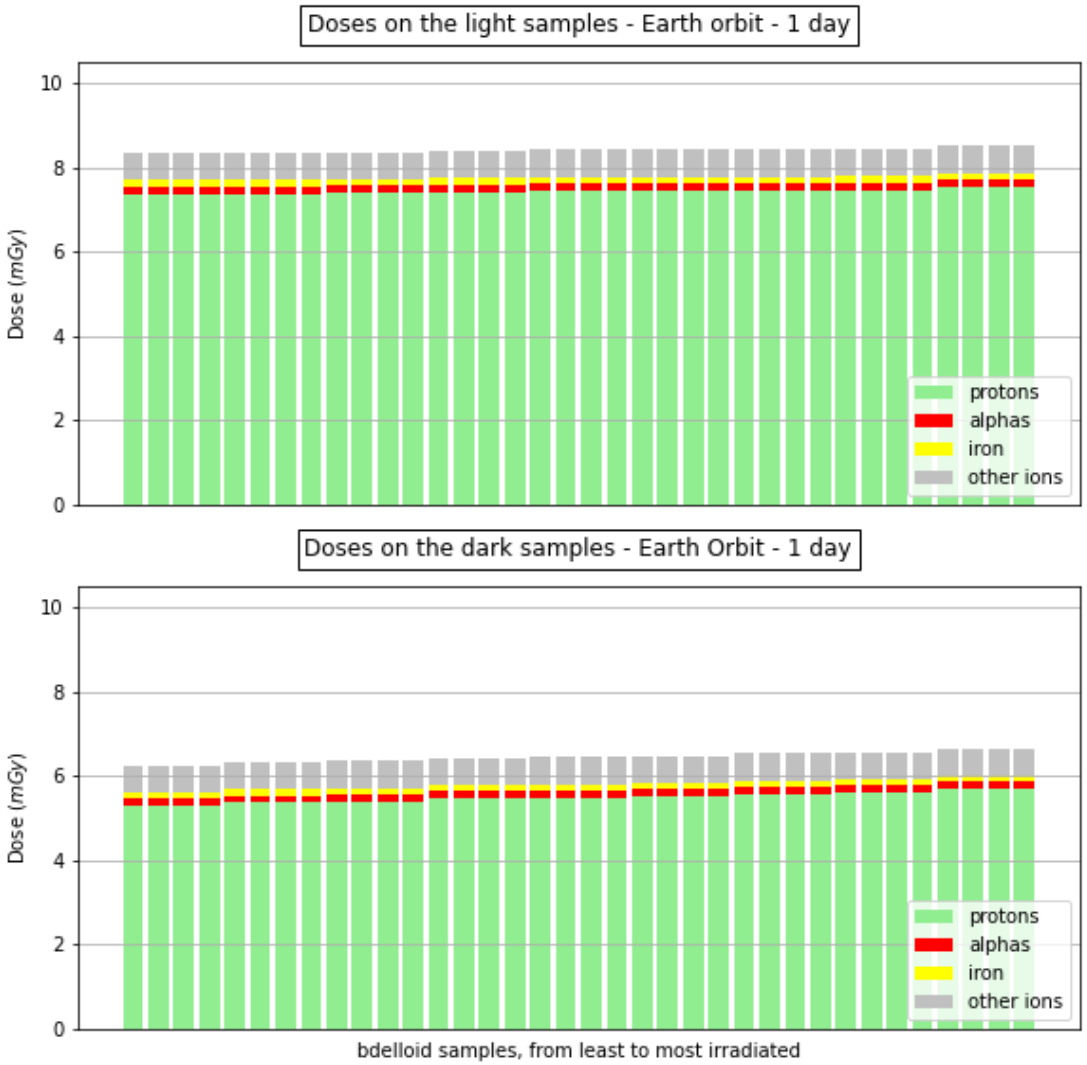

Fig. 12 Doses on the light and dark samples for the Earth orbit. The samples are sorted from least irradiated to most irradiated. The contribution of the different particles is highlighted in green for protons, red for alphas, yellow for iron and grey for the other ions. Others refers to the ions from the GCR spectrum and neutrons from the trapped model that can be seen on Fig. 6.

Lunar surface

The Lunar surface outputs smaller doses than the Earth orbit for both Oltaris and Topas. The results are presented in Fig 13. For the light patches, Oltaris gives 9.718 ± 0.021 mGy for lights and 9.376 ± 0.006 mGy for darks. The Topas simulation outputs daily doses of 3.93 mGy for the light patches and 3.90 mGy for the dark patches, which, extrapolated, give a monthly dose of 117.9 mGy for the lights and 117.0 mGy for the darks. It presents a different pattern of dose contribution. Although proton, alphas and iron ions still make more than half of the contribution, the other particles take a significant percentage of the total dose (>43%). The GCR is the main contributor to the total dose ($\approx$ 80%)

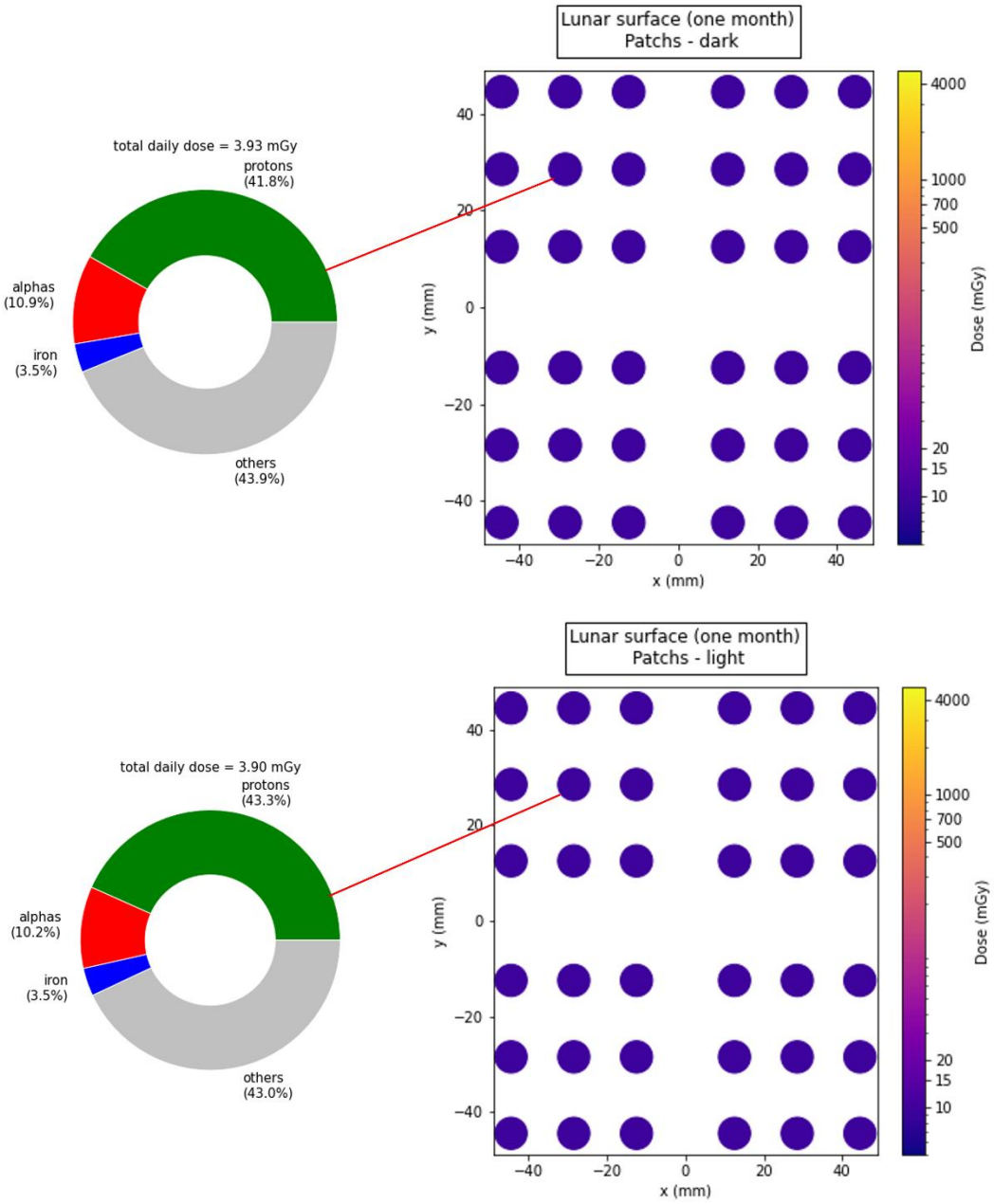

Fig. 13 Results of Oltaris and Topas for the lunar surface environment. The right colormaps, obtained with Oltaris, show the irradiation of the rotifer samples, whereas the pie charts on the left, obtained with Topas, differentiate the contribution of the different particles. For this environment, the protons and GCR ions are the main source of radiation. The color bar scale is common for all environments. Others refers to the light particles from the Moon albedo and ions from the GCR spectrum that can be seen on Fig. 7.

Mars surface

For the Martian surface, Oltaris outputs 8.405 ± 0.071 mGy for the light samples and 8.459 ± 0.008 mGy for the dark samples. These results are represented in Fig. 14. Topas gives 2.76 mGy per day for the light patches and 2.72 for the dark patches, that can be extrapolated in a monthly dose of 82.8 mGy and 81.6 mGy respectively, making the Mars environment the least irradiating in terms of raw dose output. In the Martian environment, the doses contribution is equally brought by protons and other particles, while iron and alpha contributions are negligible.

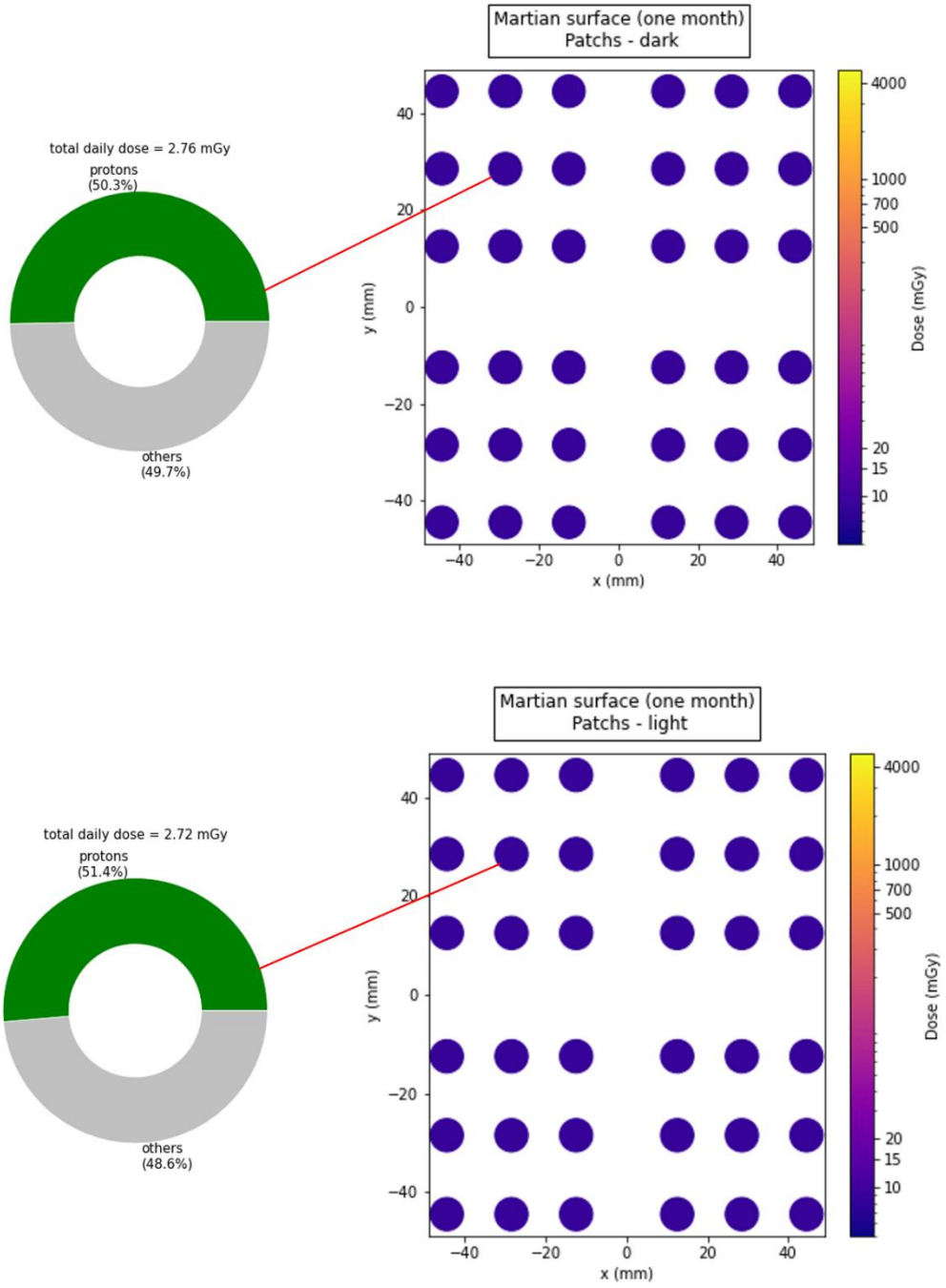

Fig. 14 Results of Oltaris and Topas for the Martian surface environment. The right colormaps, obtained with Oltaris, show the irradiation of the rotifer samples, whereas the pie charts on the left, obtained with Topas, differentiate the contribution of the different particles. For this environment, protons and other particles excluding iron and alphas are the main source of radiation. The color bar scale is common for all environments. Others refers to the ions from the GCR spectrum and light particles from the Martian albedo that can be seen on Fig. 8.

SPE

SPE simulation results are presented in Fig. 15. The doses attained are the highest of all simulations, with an average of 4536.111 ± 277.017 mGy for the light samples and 659.255 ± 21.72 mGy for the dark samples. The striking difference between light and dark samples is likely due to the shielding of the dark samples. The many less energetic protons present in the SPE (c.f. Fig. 9) are stopped within the light patches or the shielding of the module. The Topas simulations have been run with a fraction of the SPE environment due to

computational limitations. SPE are solely protons, which explains the Topas repartition pattern (>99% protons for light and dark samples), with a small contribution of secondary particles such as gamma rays created within the module. Assuming that the 1989 October SPE event lasted 21 days (from 20th of October until 10th of November according to Fig 2 of section 1), the total number of particles was divided by 1440 which corresponds approximately to 20 minutes of exposition. The corresponding dose output is 39.19 mGy for the lights, and 6.36 mGy for the darks, which corresponds for the total event to 56,433 mGy for the lights and 9,158 mGy for the darks.

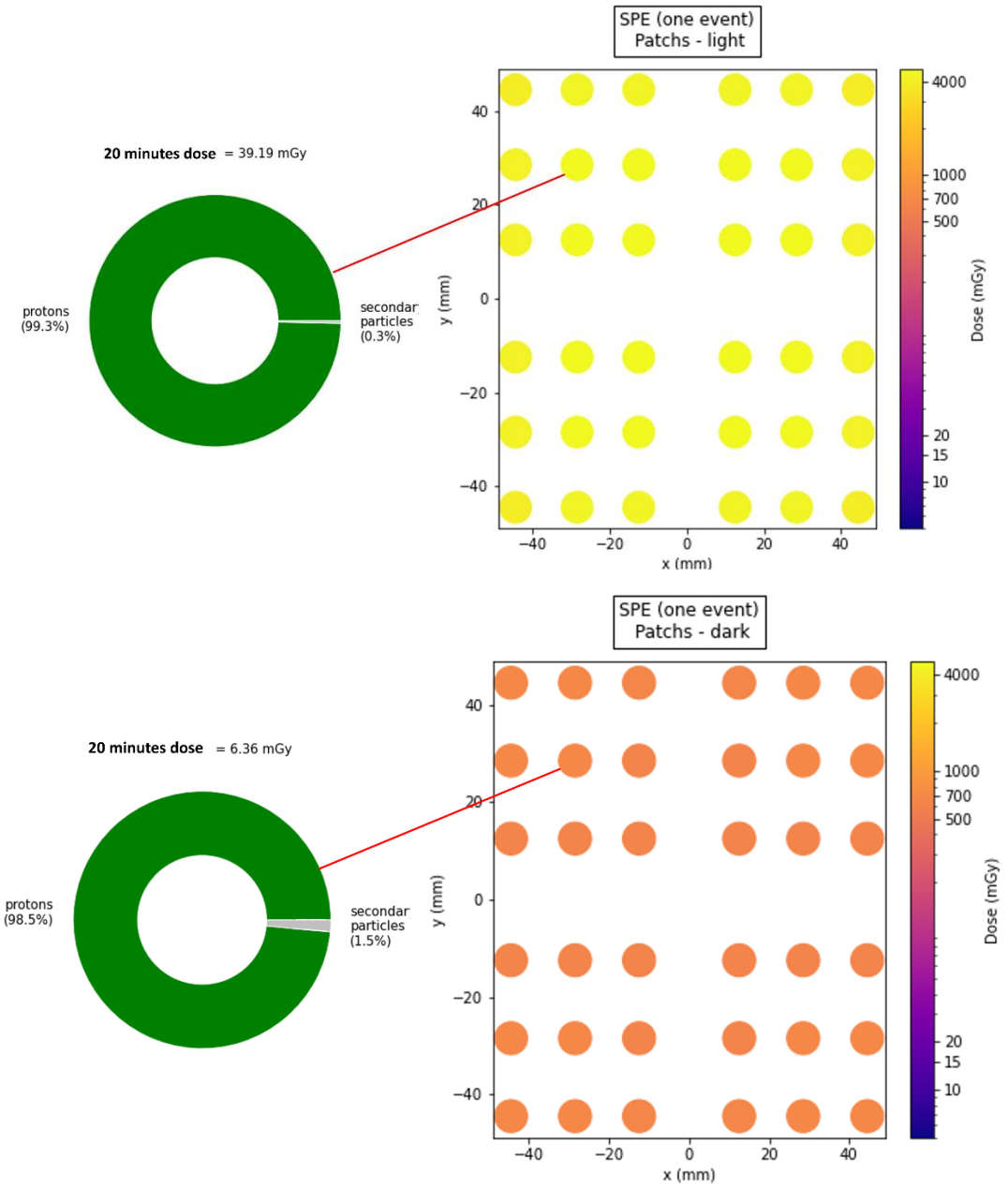

Fig. 15 Results of Oltaris and Topas for the SPE event. The right colormaps, obtained with Oltaris, show the irradiation of the rotifer samples, whereas the pie charts on the left, obtained with Topas, differentiate the contribution of the different particles. For this environment, protons completely dominate the dose output.

Discussion

For Earth orbit, lunar and Martian surface, computed doses have a similar order of magnitude, ranging from 8.41 mGy/month (light patches on Mars) to 13.6 mGy/month (light patches on Earth orbit) for Oltaris and 2.72 mGy/day (dark patches on Mars) to 8.52 mGy/day (light patches on Earth) for Topas. The doses are homogeneous among the samples. The light samples are slightly more irradiated than the dark ones, except for the Mars surface whose dark samples scored 8.46 mGy/month and light samples scored 8.41 mGy/month in Olatris. Due to the presence of the Van Allen belt, described by the AP8 model contributing for 78% of the total dose output, the Earth orbit is the most damaging environments out of the three. The Earth orbit outputs support the choice of studying proton and iron irradiation on the ground. More particularly, protons are responsible for most of the dose deposition. With iron and alpha, they cover 90% of the dose output. Consequently, it would be interesting to study the resistance of rotifers to alpha radiation on ground. In the case of Moon and Mars surface however, the contribution of light and heavy ions from the GCR and albedo components are to consider as they contribute up to 49.7% of the total dose outputs. Subsequent simulations could further differentiate the contribution to the total dose, particle by particle, to achieve a more comprehensive understanding of what particles contribute most.

The actual determining factor in term of survival of the rotifers would not be the GCR, trapped or albedo environments but SPEs. Indeed, although SPEs are occasional and unpredictable, they are the most dose inducing elements of space environments, with up to 56 Gy by event according to Topas. However, SPE are also the events for which the shielding of the dark samples is the most efficient, reducing the doses by a factor 7. Furthermore, the ISS could function as an additional radiation shield that could further reduce the dose outputs, although producing secondary particles that need consideration.

There is a striking difference between the Topas computed doses compared to the Oltaris computed doses. Topas doses are systematically one order of magnitude above the ones provided by Oltaris. A first hypothesis to explain this difference is the different material definition used for the rotifers in Topas and in Oltaris. Indeed, Oltaris uses a $C_6HN_7O_8$ with a 1.1 g/cm^3 density tissue, whereas Topas uses a $C_{200}Cl_3H_{100}KN_{40}Na_2O_{650}S_2$ with 1.09 g/cm^3 density human skin material. To investigate the energy deposition difference between the two materials, SRIM (Ziegler 1999) has been used to retrieve energy deposition tables of protons, since they have the most important contribution to total dose, in the two materials. The energy deposition per unit of length, dE/dx, is closer than what would be expected for such differences in doses: 4.4231 MeV/mm for 10 MeV protons in Oltaris Tissue and 5.028 MeV/mm for 10 MeV protons in Topas material which is indeed greater but not comparable to the 7-factor reported between Oltaris and Topas. Another possibility would be that Oltaris environments are retrieved at the center of the samples. When implemented in Topas, particles are reemitted from a sphere outside of the sample. Therefore, they lose additional energy to penetrate in the rotifer patches, which can lead to a higher energy deposition output. To further investigate the Oltaris and Topas differences, Oltaris' Tissue material could be recreated in Topas to conduct a cross-checking simulation and compare the results.

The overall environmental doses experienced by the rotifers in space are relatively low compared to their remarkable resistance to ionizing radiation. Therefore, there is optimism that

the rotifers will survive after spending a few months outside of the International Space Station (ISS). The primary source of radiation that poses a significant threat is solar particle events (SPEs). As mentioned in section 1, there are approximately 7 SPEs per year during solar maximum activity. To investigate the potential survival time of rotifers in space, we can consider a worst-case scenario. Using the Topas estimation of 255.6 mGy per month as an upper limit for the dose in Earth's orbit, we can calculate the total annual dose. For each light sample, the SPEs contribute up to 56 Gy, while for dark samples, it is 9.2 Gy. This results in a total annual dose of 395 Gy for light and 67.4 Gy for dark patches (with ≈3 Gy due to the Earth orbit environment and the rest due to SPEs). It is important to emphasize that relying solely on the raw total Gy output may not provide the most relevant information for drawing biological conclusions, as it combines various types of radiation. However, since most of the contribution comes from proton, we will consider the proton survival limits of the rotifers in the following analysis. In section 2, we highlighted the threshold for 50% of the population to be sterilized: about 453 Gy for 4 MeV proton radiation (Hespeels et al. 2020) bdelloids can survive up to 5000 Gy of proton radiation. It would then take 14 months for half of the light rotifers to be sterilized and almost 7 years for the dark rotifers. To kill the individuals however, it would take almost 13 years for the light samples and 74 years for the dark ones. To illustrate these values with an example, consider that the bdelloids module could travel during extreme and frequent SPE events from Earth to Moon (72 hours[2], (Loff 2015) to Mars (7 months[3] (« Trip to Mars - NASA Mars » 2023)) and return all the way back to Earth alive with most of the individuals fertile.

Similar conclusions can be achieved for Martian and Lunar environments as most of the dose contribution comes from SPE. A similar worst case scenario conditions on the Moon would give a yearly dose of 393.4 Gy and 392.99 Gy on Mars for the light samples, with only 1.4 Gy and 0.99 Gy respectively without the SPEs.

It is crucial however to acknowledge that these conclusions are subject to change due to the incompleteness of our model. The rotifers have demonstrated vulnerability to UV radiation and temperature variations (C. Ricci et al. 2005). UV and temperature changes can prove to be more harmful than radiation, as increased temperatures can cause the unfolding of proteins in rotifers, leading to a loss of their functionality.

We conclude our analysis with a critical evaluation of our model. The disparities between Oltaris dose outputs and Topas have been previously highlighted, along with preliminary suggestions for further investigation. From a broader perspective, understanding and validating simulation outputs are of paramount importance. In this regard, we would like to share several general principles derived from this research to aid future investigations.

First and foremost, it is essential to avoid pursuing perfection. In its current state, the module model is incomplete due to a lack of details in the documentation. For instance, the SM2 module is currently floating within the CM. While achieving precise and realistic modeling of the SM2 is preferable, it was crucial to promptly develop a functional prototype to assess the overall workflow's efficacy. Numerous adjustments and data transformations are involved at each stage of the process, ranging from module modeling in Topas to geometry raytracing, XML translation, simulation setup in Oltaris, environment and dose retrieval, Oltaris environment

[2] Based on the Apollo missions averaged travel duration

[3] Based on NASA's Cruise spacecraft

translation to Topas sources, and analysis of Topas outputs with graphical representation of results. The advantage of initiating first a basic but complete workflow proves more beneficial as it allows to follow the complete workflow and enables prompt identification and anticipation of errors, exceptional cases, and limitations. Furthermore, dedicating substantial effort to a particular design philosophy, only to discover its incompatibility with subsequent workflow stages, leads to significant time and resource wastage.

Other ways of improving the reliability of the simulation imply robustness testing, documentation, and continuous improvement. On the module raytracing stage, various robustness testing has been performed. These imply to test extremes cases that have led for instance to the discovery of rounding errors, highlighting the need to implement a tolerance parameter. Documenting and explaining textually a code or simulation setup for each version helps detect some overlooked design or computational mistakes. For instance, the Oltaris environment fluences are normalized in cm^2. When documenting the code to implement them in Topas, we realized that they were multiplied by a m^2 surface (the standard unit in Topas), an error overlooked in the initial coding. Finally, it is important to note that simulations and code can be continuously improved and refined, based on feedback. By regularly revisiting and refining simulation models, results validation enhances both accuracy, robustness, and reliability.

Conclusion

This master thesis simulated the effects of radiation exposure on bdelloid rotifers by reproducing ground-based experiments and spatial radiative environments.

The second section of the master thesis reproduced ground based experiments from Hespeels et al. (2020) to determine if all nuclei are equally affected by the radiation, or if some rotifers are partially or entirely unaffected. The experimental geometries were reproduced in Topas, and the findings indicated that all individuals, cells, and nuclei were damaged at specific doses of 4 MeV protons (at 3.00 Gy), 0.5 GeV/n ^{56}Fe (at 53.00 Gy), and X-rays (at $2.67x10^{-2}$ Gy). This rule out the possibility of unaffected rotifers or germinal cells in previous studies, as all administrated doses were above those thresholds. Furthermore, simulations revealed significant differences between low and high LET radiation in term dose deposition pattern on nuclei. High LET radiation showed concentrated energy deposition patterns, whereas low LET radiation was more diffuse. In conclusion, the simulations support the idea that reduced fertility observed in samples is associated with energy deposition quantity and complexity, rather than the absence of damage. The section has been submitted as an article to Hydrobiologia and is currently revised for publication.

The third part of the study aimed to assess the impact of space radiative environments on rotifers by conducting simulations to evaluate the dose they receive. To facilitate this, a Python-based rotifer module was developed and integrated into Oltaris using a raytracing process. Oltaris was utilized to retrieve four space environments and estimate the corresponding doses: Earth orbit (ISS trajectory), Lunar surface, Mars surface, and solar particle event (SPE). The environments were implemented in Topas to retrieve additional dose estimations and differentiate the contribution of diverse particles. The simulation results indicated that the rotifers received a maximum dose of 255.6 mGy/month in Earth orbit, 117.9 mGy/month on the Martian surface, 82.8 mGy/month on the Lunar surface, and 54.4 Gy/event during the SPE. Notably, there was a significant difference between the dose estimations obtained from Oltaris and Topas, with

Topas showing a factor of 7 higher outputs, possibly due to a difference of material used in dose calculation and simulation bias induced by the implementation of Oltaris environment in Topas source. Among the parameters studied, the SPEs emerged as the most critical factor influencing the survival of the rotifers. We presented a worst-case scenario, where the most exposed individuals in Earth orbit experienced doses of 395 Gy/year. Under these conditions, the rotifers exhibited a fertility time limit of 14 months and a lifespan of 13 years. However, with appropriate protection measures in place, these values could be increased to 7 and 74 years, respectively. This makes rotifers an ideal model organism for investigating the long-term effects of space exposure on living organisms. In order to enhance the reliability and accuracy of the simulations, we discussed several ideas for future improvements, including a detailed investigation of the discrepancies between Topas and Oltaris outputs. By addressing these factors, we can further advance our understanding of the effects of space radiative environments on organisms and ensure more precise simulations in future studies.

References

Agostinelli, S., J. Allison, K. Amako, J. Apostolakis, H. Araujo, P. Arce, M. Asai, et al. 2003. « Geant4—a Simulation Toolkit ». *Nuclear Instruments and Methods in Physics Research Section A: Accelerators, Spectrometers, Detectors and Associated Equipment* 506 (3): 250-303. https://doi.org/10.1016/S0168-9002(03)01368-8.

Allison, J., K. Amako, J. Apostolakis, H. Araujo, P. Arce Dubois, M. Asai, G. Barrand, et al. 2006. « Geant4 Developments and Applications ». *IEEE Transactions on Nuclear Science* 53 (1): 270-78. https://doi.org/10.1109/TNS.2006.869826.

Allison, J., K. Amako, J. Apostolakis, P. Arce, M. Asai, T. Aso, E. Bagli, et al. 2016. « Recent Developments in Geant4 ». *Nuclear Instruments and Methods in Physics Research Section A: Accelerators, Spectrometers, Detectors and Associated Equipment* 835 (november): 186-225. https://doi.org/10.1016/j.nima.2016.06.125.

Almahwasi, Ashraf. 2016. « Does Hadron Therapy Offer Enough Effectiveness in Treating Cancer to Be Worth the Cost? » *ResearchGate*, 2016. https://doi.org/10.13140/RG.2.2.35789.64482.

Angelis, G. De, Martha S. Clowdsley, Robert C. Singleterry, et J. W. Wilson. 2004. « A New Mars Radiation Environment Model with Visualization ». *Advances in Space Research* 34 (6): 1328-32. https://doi.org/10.1016/j.asr.2003.09.059.

Badavi, F., Katie J. West, J. Nealy, John W. Wilson, B. Abrahms, et N. Luetke. 2006. « A Dynamic/Anisotropic Low Earth Orbit (LEO) Ionizing Radiation Model ». 2006. https://www.semanticscholar.org/paper/A-Dynamic-Anisotropic-Low-Earth-Orbit-(LEO)-Model-Badavi-West/6abbbf6139e2487e2b303547242a2df35bf44fb8.

Biermann, Peter, et Guenter Sigl. 2002. « Introduction to Cosmic Rays ». arXiv. http://arxiv.org/abs/astro-ph/0202425.

Chancellor, Jeffery, Craig Nowadly, Jacqueline Williams, Serena Aunon-Chancellor, Megan Chesal, Jayme Looper, et Wayne Newhauser. 2021. « Everything You Wanted to Know about Space Radiation but Were Afraid to Ask ». *Journal of Environmental Science and Health. Part C, Toxicology and Carcinogenesis* 39 (2): 113-28. https://doi.org/10.1080/26896583.2021.1897273.

Clowdsley, Martha, John Nealy, John Wilson, Brooke Anderson, Mark Anderson, et Shawn Krizan. 2005. « Radiation Protection for Lunar Mission Scenarios », february. https://doi.org/10.2514/6.2005-6652.

« Environment Source — TOPAS 3.8 documentation ». 2022. 2022. https://topas.readthedocs.io/en/latest/parameters/source/environment.html.

« estar-stopping power and range tables for electrons ». 2023. 2023. https://physics.nist.gov/PhysRefData/Star/Text/ESTAR.html.

Foelsche, T., R. B. Mendell, J. W. Wilson, et R. R. Adams. 1974. « Measured and Calculated Neutron Spectra and Dose Equivalent Rates at High Altitudes; Relevance to SST Operations and Space Research », january. https://ntrs.nasa.gov/citations/19740027106.

« Geant4 Documentation ». 2023. Geant4. 2023. https://geant4.web.cern.ch//docs/.

Gruber, Manuel. 2014. « Propriétés Électroniques et Magnétiques d'interfaces Hybrides : Des Molécules Isolées Aux Films Moléculaires Ultra-Minces Sur Des Substrats Métalliques ». Strasbourg. https://www.researchgate.net/publication/281185409_Proprietes_electroniques_et_magnetiques_d'interfaces_hybrides_des_molecules_isolees_aux_films_moleculaires_ultra-minces_sur_des_substrats_metalliques.

Hespeels, Boris, Diego Fontaneto, Valérie Cornet, Sebastien Penninckx, Jérémy Berthe, Lucie Bruneau, James W. Larrick, et al. 2023. « Back to the roots, desiccation and radiation resistances are ancestral characters in bdelloid rotifers | BMC Biology | Full Text ». *BMC Biology*, 2023. https://bmcbiol.biomedcentral.com/articles/10.1186/s12915-023-01554-w.

Jiggens, Piers, Marc-Andre Chavy-Macdonald, Giovanni Santin, Alessandra Menicucci, Hugh Evans, et Alain Hilgers. 2014. « The Magnitude and Effects of Extreme Solar Particle Events ». *Journal of Space Weather and Space Climate* 4: A20. https://doi.org/10.1051/swsc/2014017.

King, Joseph H. 2012. « Solar Proton Fluences for 1977-1983 Space Missions ». *Journal of Spacecraft and Rockets*, mai. https://doi.org/10.2514/3.62088.

Leroy, Claude, et Pier-Giorgio Rancoita. 2016. *Principles of radiation interaction in matter and detection*. 4th edition. New Jersey: World Scientific.

Loff, Sarah. 2015. « The Apollo Missions ». Text. NASA. 16 march 2015. http://www.nasa.gov/mission_pages/apollo/missions/index.html.

« NASA - Space Radiation Analysis Group (SRAG) Web Site ». 2023. Terrie Bevill. 2023. https://srag.jsc.nasa.gov/.

Nikjoo, Hooshang, Shuzo Uehara, et Dimitris Emfietzoglou. 2016. *Interaction of Radiation with Matter*. 0 éd. CRC Press. https://doi.org/10.1201/b12109.

« OLTARIS Home Page ». 2023. 2023. https://oltaris.nasa.gov/login.

O'Neill, P. M. 2006. « Badhwar–O'Neill Galactic Cosmic Ray Model Update Based on Advanced Composition Explorer (ACE) Energy Spectra from 1997 to Present ». *Advances in Space Research*, Space Life Sciences: Flight Measurements, Calibration of Detectors and Environmental Models for Radiation Analysis, 37 (9): 1727-33. https://doi.org/10.1016/j.asr.2005.02.001.

Penninckx, Sebastien. 2023. « Interaction rayonnement-matière vivante ». In *SPHYM101*. UNamur.

Perez, Jason. 2017. « Why Space Radiation Matters ». Text. NASA. 13 april 2017. http://www.nasa.gov/analogs/nsrl/why-space-radiation-matters.

Rabbow, Elke, Petra Rettberg, Simon Barczyk, Maria Bohmeier, Andre Parpart, Corinna Panitz, Gerda Horneck, et al. 2015. « The Astrobiological Mission EXPOSE-R on Board of the International Space Station ». *International Journal of Astrobiology* 14 (1): 3-16. https://doi.org/10.1017/S1473550414000202.

Rabbow, Elke, Petra Rettberg, Andre Parpart, Corinna Panitz, Wolfgang Schulte, Ferdinand Molter, Esther Jaramillo, René Demets, Peter Weiß, et Rainer Willnecker. 2017. « EXPOSE-R2: The Astrobiological ESA Mission on Board of the International Space Station ». *Frontiers in Microbiology* 8. https://doi.org/10.3389/fmicb.2017.01533.

« Rotifer-in-Space.Com ». 2023. Rotifer in Space. 2023. http://rotifer-in-space.com/.

Schlickeiser, Reinhard. 2010. *Cosmic Ray Astrophysics*. 1. ed., corr. 2. print.; [Nachdr. der Ausg.] 2003. Astronomy and Astrophysics Library. Berlin: Springer.

Seibert, J. Anthony, et John M. Boone. 2005. « X-Ray Imaging Physics for Nuclear Medicine Technologists. Part 2: X-Ray Interactions and Image Formation ». *Journal of Nuclear Medicine Technology* 33 (1): 3-18.

Singleterry, Robert C., Steve R. Blattnig, Martha S. Clowdsley, Garry D. Qualls, Christopher A. Sandridge, Lisa C. Simonsen, John W. Norbury, et al. 2010. « OLTARIS: On-Line Tool for the Assessment of Radiation in Space », january. https://ntrs.nasa.gov/citations/20100027428.

Slaba, Tony, et K. Whitman. 2020. « The Badhwar-O'Neill 2020 GCR Model ». *Space Weather* 18 (june). https://doi.org/10.1029/2020SW002456.

Townsend, L. W., E. Neal Zapp, D.L. Stephens, et J.L. Hoff. 2003. « Carrington Flare of 1859 as a Prototypical Worst-Case Solar Energetic Particle Event ». *IEEE Transactions on Nuclear Science*, december 2003.

« Trip to Mars - NASA Mars ». 2023. 2023. https://mars.nasa.gov/mars2020/timeline/cruise/.

« Very High-Energy Electrons for Cancer Therapy ». 2020. CERN Courier. 15 december 2020. https://cerncourier.com/a/very-high-energy-electrons-for-cancer-therapy/.

Wilson, J. W., F.A. Cucinotta, M.J. Golightly, J. Nealy, Garry D. Qualls, Francis F. Badavi, G. De Angelis, et al. 2006. « International Space Station: A Testbed for Experimental and Computational Dosimetry ». *Advances in Space Research* 37 (9): 1656-63. https://doi.org/10.1016/j.asr.2005.02.038.

Wilson, J. W., L. W. Townsend, et H. Farhat. 1989. « Cosmic-Ray Neutron Albedo Dose in Low-Earth Orbits ». *Health Physics* 57 (october): 665-68.

Wilson, John, et Fred denn. 1976. « Preliminary analysis of the implications of natural radiations on geostationary operations ». *NASA STI/Recon Technical Report N* 76 (august): 33120.

Yong, Ching, Tharek Rahman, et Kim Mey Chew. 2015. « Wireless industry emission: Electromagnetic field monitoring and analysis » 10 (january): 9800-9807.

Ziegler, J F. 1999. « The Stopping of Energetic Light Ions in Elemental Matter ». *J. Appl. Phys*.

Appendix: module reference blueprints

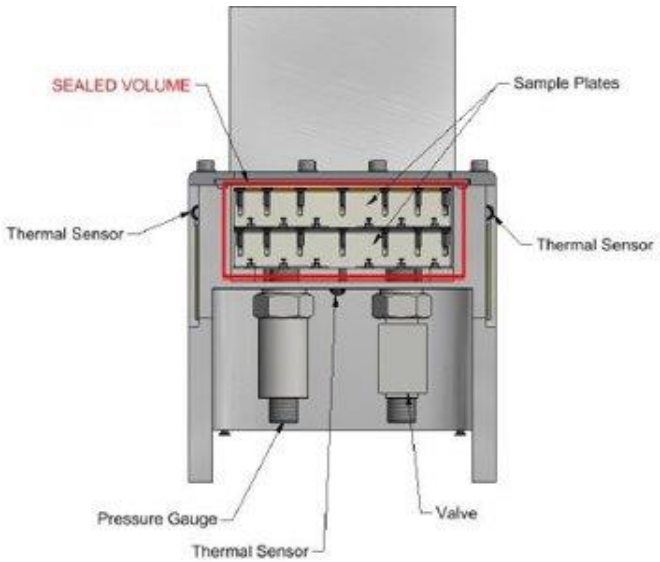

Figure 128: Carrier container

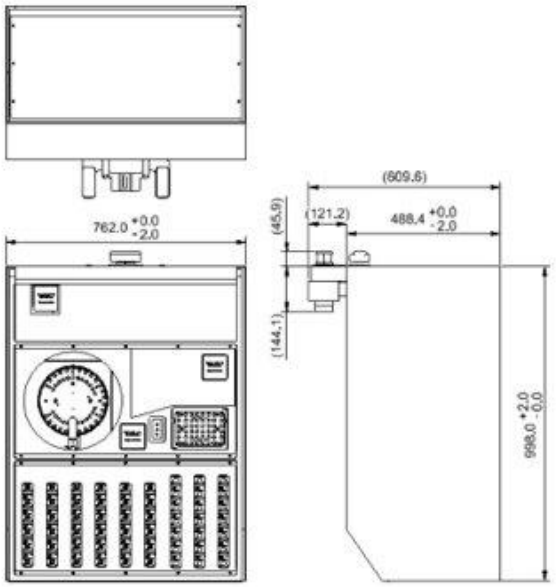

Figure 42: EXPO SM1 configuration overall dimensions

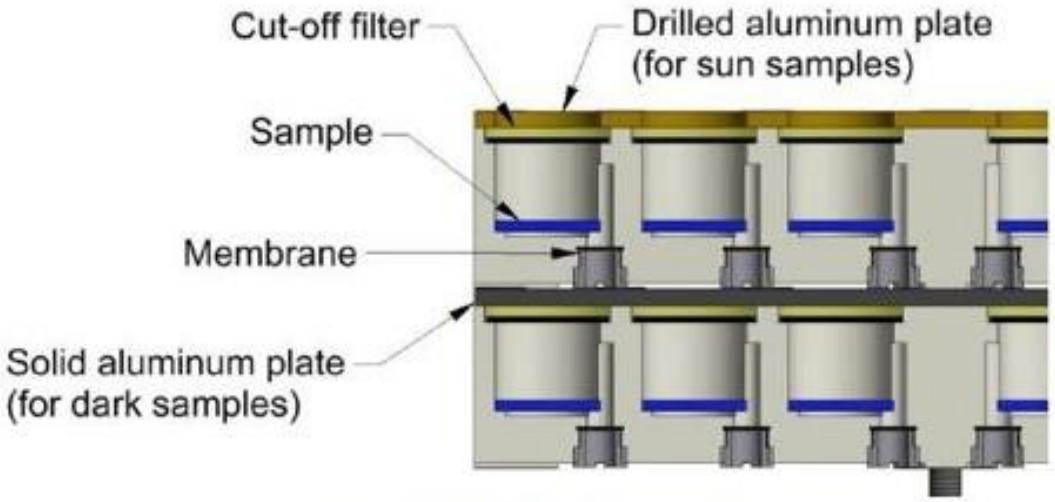

Figure 126: MEXEM well concept